https://doi.org/10.57634/RCR5058

Synthesis and plasmonic tuning of gold and gold–silver nanoparticles

Nikolai G. Khlebtsov,[a,b] **Lev A. Dykman,**[a] **Boris N. Khlebtsov** [a]

[a] *Institute of Biochemistry and Physiology of Plants and Microorganisms, Saratov Scientific Centre of the Russian Academy of Sciences, prosp. Entuziastov 13, 410049 Saratov, Russian Federation*
[b] *Saratov State University, ul. Astrakhanskaya 83, 410012 Saratov, Russian Federation*

Plasmonic particles represent a rapidly developing material for nanotechnology. They are used in biomedicine as sensoric, diagnostic and therapeutic agents. Most theranostic applications exploit the unique optical properties of gold or hybrid nanoparticles in which visible or near-infrared light excites localized plasmon resonances. The review discusses the latest advances in the synthesis of the most popular and sought-after nanoparticles such as gold nanospheres, nanorods, nanoshells, nanocages and nanostars and also gold–silver nanorods and nanocuboids. The consideration is focused on the design principles of particle size, shape and structure, which provides for desired tuning of optical properties such as plasmon resonance wavelength and absorption and scattering cross-sections. The optimal parameters of the particles for the use in the photothermal and photodynamic therapy, surface-enhanced Raman scattering and catalysis are discussed. The bibliography includes 294 references.

Contents

1. Introduction 1
2. General principles of plasmon resonance tuning 2
3. Methods for synthesis of large monodisperse gold nanospheres 6
4. Synthesis and optical tuning of gold nanorods 9
5. Gold nanoshells and nanocages 14
6. Gold nanostars 16
7. Gold nanorods with a silver shell 17
8. Applications of nanoparticles of various size, shape and structure 20
9. Conclusion 23
10. List of abbreviations and symbols 24
11. References 25

1. Introduction

The unique physicochemical properties of gold nanoparticles (GNPs) depending on their size, shape and composition are widely utilized in various fields of modern science: nanomedicine, nanoelectronics, nanocatalysis, nanophotonics, nanoplasmonics and nanosensorics.[1–6] To date, robust methods have been developed for the synthesis of GNPs of various sizes and shapes and multicomponent structures.[7,8] Modern techniques have been elaborated for the preparation of multifunctional nanoparticles *via* modification of particles by various molecules to endow them with desired physicochemical and biological properties.[9] Functionalized GNPs have found a multitude of promising applications in modern biomedicine: they are used in chemical and biological analytics, optical and optoacoustic bioimaging, targeted delivery of drugs and target molecules, *etc*. The stage of laboratory research of GNPs is being advanced to practical application in diagnosis and therapy; for example, protocols of photothermal therapy (PTT) combined with photodynamic therapy (PDT), chemotherapy, immunotherapy, gene therapy and radiotherapy have been developed.[10,11]

Studies of GNPs have a long history;[12–14] however, the modern understanding of physics that determines their remarkable optical properties was attained owing to the development of the plasmonic concept, which relates the enormous near- and far-field enhancement to the localized plasmon resonance (PR) in noble metal nanoparticles. By varying the shape and structure of GNPs, it is possible to tune the PR wavelength from visible to near-IR range of the electromagnetic radiation spectrum, thus avoiding the

N.G.Khlebtsov. Doctor of Physical and Mathematical Sciences, Honoured Scientist of the Russian Federation, Head of Laboratory of Nanobiotechnology of IBPPM RAS, Professor of the Department of Materials Sciences, Technology and Quality Management of SSU.
E-mail: khlebtsov@ibppm.ru
Current research interests: biophotonics and nanobiotechnology of plasmon resonance particles, biomedical applications of metal nanoparticles, static and dynamic light scattering by small particles and clusters, and programming and computer simulation of light scattering and absorption by various metallic and dielectric nanostructures.
L.A.Dykman. Doctor of Biological Sciences, Leading Researcher of the Laboratory of Immunochemistry of IBPPM RAS.
E-mail: dykman@ibppm.ru
Current research interests: immunochemistry, fabrication of gold nanoparticles, applications of gold nanoparticles in biological and medical studies, interaction of nanoparticles and conjugates with immunocompetent cells and delivery of the engineered particles to target organs, tissues and cells.
B.N.Khlebtsov. Doctor of Physical and Mathematical Sciences, Leading Researcher of the Laboratory of Nanobiotechnology of IBPPM RAS.
E-mail: khlebtsov_b@ibppm.ru
Current research interests: nanobiotechnology, plasmonics; biophotonics; fabrication, functionalization and biomedical applications of metal nanoparticles and multifunctional nanoparticles.

Translation: Z.P.Svitanko

Received 30 June 2021

© 2022 Uspekhi Khimii, ZIOC RAS, Russian Academy of Sciences

drawbacks of many other optical probes. It is noteworthy that unlike silver nanoparticles,[15] GNPs, possessing unique optical properties are low-toxic or non-toxic; they can be easily functionalized by biocompatible molecules or by molecules that are not recognized by the immune system of the body.

A number of reviews were published in the last decades, summarizing the achievements in the field of chemical synthesis of various types of GNPs including nanospheres,[12] nanorods,[16–21] nanoshells,[22] nanocages[23] and nanostars.[24] However, there is still no unified approach to the control of their optical characteristics by varying chemical reaction conditions during the synthesis or modification. This important issue is addressed in only few studies (see, *e.g.*, Ref. 25).

This review is the first attempt to combine the principles of chemical synthesis of the most demanded GNPs with the physical principle of design of particle size, shape, structure and dielectric function. This combination offers opportunities for controlling optical and physicochemical properties of the obtained nanostructures. Using this approach, it is possible to tune the optical properties such as PR wavelength and the main far-field integral parameters (absorption and scattering cross-sections) and to enhance local fields and related effects, *e.g.*, surface-enhanced Raman scattering (SERS) intensity.[26]

2. General principles of plasmon resonance tuning

The optical spectra of light absorption and scattering by metal nanoparticles exhibit resonances that are absent in the spectra of macroscopic materials. These resonances arise due to the collective behaviour of free electrons excited by incident light. Plasmon resonance of a relatively small metal sphere is usually described as stated below (Fig. 1).[27–29]

The alternating electric field of the incident light induces oscillations of free electrons, and near the particle surface, uncompensated charges arise, together with the corresponding electric restoring forces, which act on electrons. The optical resonance associated with these collective electron oscillations in small particles is called localized surface plasmon resonance (LSPR), or simply PR. The term localized is used to distinguish this resonance from the propagating plasmon excitations at the metal/dielectric interface.

Although the above description is commonly used, the reference to the collective oscillations of free electrons is not quite justified from the physical standpoint, because in real problems of classical plasmonics, the electron oscillations themselves are usually behind the scenes. The term plasmon was introduced by Pines[30] to describe a quantum of elementary excitations associated with high-frequency collective oscillations of valence electrons. This term means a quasi-particle or elementary excitation of the charge density in a plasma. However, the investigation object of plasmonic problems, including far-field (absorption and scattering cross-sections) and local near-field (SERS) characteristics, is optical (electromagnetic) response of the system.

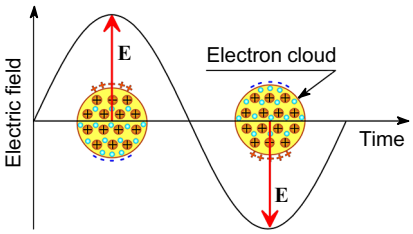


Figure 1. Schematic image of the surface PR of a small metal particle. An alternating electric field (**E**) causes coherent oscillations of the electron cloud near the equilibrium position owing to restoring forces of uncompensated charges on the surface. The Figure was adapted from Ref. 29 with permission from ACS Publications.

For classical description of this response, it is sufficient to use the dielectric function of the metal, which already phenomenologically takes into account the collective oscillations of electrons and interaction of electrons with the electromagnetic field. For example, in the dipole approximation, the field inside a small sphere is equal to $3\,\mathbf{E}_0/(\varepsilon_r+2)$, where $\mathbf{E}_0$ is the incident field vector (amplitude), $\varepsilon_r=\varepsilon/\varepsilon_m$ is the relative dielectric permittivity, ε_m is the dielectric permittivity of the medium. It can be seen that under condition $\varepsilon_r(\lambda_{PR})\simeq -2$, the internal field and related absorption would show resonance behaviour at an appropriate plasmon resonance wavelength (λ_{PR}). Despite the fact that the resonance condition is determined by a negative real part of ε_r, the amplitude of the resonance absorption cross-section is proportional to the imaginary part.

Thus, the description of a resonance behaviour by no means requires a physical consideration involving collective oscillations of electrons.† In the general case, the resonance condition is determined by many factors, including the particle shape, structure and size, particle interactions, and properties of the environment. However, for simple description of PR of single nanoparticles smaller than 30–50 nm, it is sufficient to use a combination of the dipole approximation and the Drude theory[27] for the dielectric function.

In the classical theory, the interaction of an electromagnetic wave with a particle material is described phenomenologically in terms of the optical permittivity or optical dielectric function $\varepsilon(\omega)$ (ω is the angular optical frequency), which appear in the Maxwell equations and boundary conditions. The spectral dependence is usually derived using the tabular data for bulk samples (films), which should, however, be corrected for various damping mechanisms if the particle size is <10 nm.[28,32] The spectral dependences of the real and imaginary parts of the refractive index of bulk gold and the calibration curve for determining the particle diameter from the LSPR peak position for GNPs in water are summarized in Fig. 2.

Quite a few arrays of data for the optical constants of film and single-crystalline gold samples can be found in the literature.[57] However, the vast majority of simulations of the optical properties of GNPs are based on the results of Johnson and Christy.[38] Olmon *et al.*[40] thoroughly analyzed published data and reported new spectral dependences for three types of bulk gold samples (films) — single-crystal (SC), evaporated (EV) and template-stripped (TS) samples. The surface of TS gold was much smoother than the EV film surface. The results of the two mentioned publications[38,40] are similar for the UV region, but markedly differ for the near-IR range.

Some of the published data for spectral dependences of the real and imaginary parts of the refractive index and the results of their spline interpolation[41] carried out by analogy with the procedure reported by Khlebtsov[32] (for the first version of this approximation, see Khlebtsov *et al.*[42]) are

† This issue is discussed in detail in the third chapter of a monograph.[31]

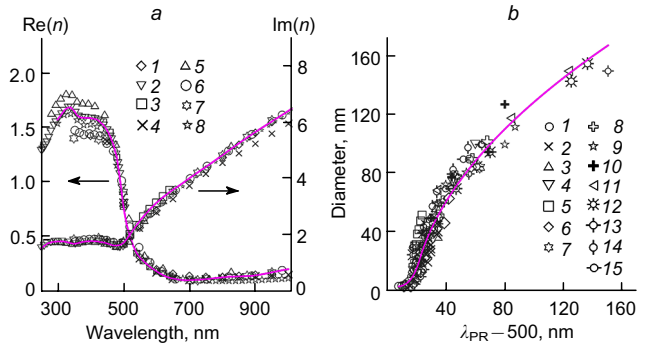


Figure 2. Spectral dependences of the real [Re(n)] and imaginary [Im(n)] parts of the refractive index of a bulk gold sample (*a*) and calibration curve for determining the particle diameter from the surface PR for GNPs in water (*b*). The points in Fig. *a* are data from Refs 33 (*1*), 34 (*2*), 35 (*3*), 36 (*4*), 37 (*5*), 38 (*6*), 39 (*7*), 40 (*8*); continuous lines are spline interpolations.[41] The continuous line in Fig. *b* shows the analytical interpolations of the experimental data from Refs 42 (*1*), 43 (*2*), 44 (*3*), 45 (*4*), 46 (*5*), 47 (*6*), 48 (*7*), 49 (*8*), 50 (*9*), 51 (*10*), 52 (*11*), 53 (*12*), 54 (*13*), 55 (*14*), 56 (*15*). The Figure was created by the authors using data of mentioned publications.

depicted in Fig. 2. For calculation of the position of PR of spherical particles, the most important range is between 520 and 580 nm; for this range, the data reporeted by Otter[35] for crystalline samples were used. The results of spectroscopy and electron microscopy were in good agreement with calculations by the Mie theory with this set of optical constants.[32]

A large body of information on the measurement of sizes and PR wavelengths for spherical particles in water is available from the literature. In Fig. 2*b*, the points represent data taken from 15 publications, and their analytical approximation is given, which can be used for easy determination of the mean particle diameter from the measured PR wavelength,

$$d\,(\text{nm}) = \begin{cases} 3 + 7.5 \times 10^{-5} X^4, & X < 23 \\ \dfrac{\sqrt{X - 16.7} - 1}{0.063}, & X \geqslant 23 \end{cases} \qquad (1)$$

$$X = \lambda_{\text{PR}}(\text{nm}) - 500$$

Unlike the approximation proposed by Khlebtsov,[32] Eqn (1) is applicable up to a particle diameter of 160 nm.

If the particle size is comparable with the effective mean free path of electrons (l_{eff}), the dielectric function of the particle is size-dependent [$\varepsilon_{\text{p}}(\omega, l_{\text{eff}})$], as distinct from the dielectric function of the bulk sample [$\varepsilon_{\text{b}}(\omega)$]. According to Kreibig and Genzel,[58] the size-dependent correction of the tabular function $\varepsilon_{\text{b}}(\omega)$ can be introduced according to the classical Drude model

$$\varepsilon_{\text{p}}(\omega, l_{\text{eff}}) = \varepsilon_{\text{b}}(\omega) + \Delta\varepsilon(\omega, l_{\text{eff}}) \qquad (2)$$

$$\Delta\varepsilon(\omega, l_{\text{eff}}) = \frac{\omega_{\text{p}}^2}{\omega^2 + \text{i}\omega\gamma_{\text{b}}} - \frac{\omega_{\text{p}}^2}{\omega^2 + \text{i}\omega(\gamma_{\text{b}} + \gamma_{\text{s}})} \qquad (3)$$

where $\text{i} = \sqrt{-1}$, ω_{p} is the plasma frequency;[27] γ_{b} is the damping constant for a bulk sample of gold, the parameter $\gamma_{\text{s}} = \gamma_{\text{s}}(l_{\text{eff}})$ takes into account contributions of three processes: radiative damping ($\gamma_{\text{s}}^{\text{rad}}$), electron scattering from the particle surface ($\gamma_{\text{s}}^{\text{surf}}$) and the chemical interface damping ($\gamma_{\text{s}}^{\text{CID}}$, CID) [59, 60]

$$\gamma_{\text{s}} = \gamma_{\text{s}}^{\text{rad}} + \gamma_{\text{s}}^{\text{surf}} + \gamma_{\text{s}}^{\text{CID}} \qquad (4)$$

Radiative damping is proportional to the volume, being negligibly low for small particles. The contribution of the electron scattering from the surface is usually inversely proportional to the size; the contribution of $\gamma_{\text{s}}^{\text{CID}}$ is also inversely proportional to the size, since the interaction of s-electrons with the adsorbed molecules is proportional to the volume, and the number of adsorbate molecules is proportional to the surface area. For small spherical particles, Eqn (4) can be represented in the following general form:

$$\gamma_{\text{s}} = \frac{A_{\text{s}} v_{\text{F}}}{l_{\text{eff}}} \qquad (5)$$

where v_{F} is the Fermi velocity; the damping constant A_{s} includes all possible damping mechanisms listed above.

The above classical way of taking account of size effects has a number of shortcomings, the discussion of which is beyond the scope of this review. We refer the readers to paper by Xu *et al.*,[61] who proposed an original model of size-dependent polarizability and discussed other approaches, including quantum mechanical ones.[62, 63]

In Eqn (5), the effective mean free path is proportional to particle size; for small spheres, it is often taken that $l_{\text{eff}} = a$ (a is the particle radius). Coronado and Schatz[64] proposed a versatile approximate formula to estimate the mean free path

$$l_{\text{eff}} = \frac{4V}{S} \qquad (6)$$

This formula is applicable to particles of a simple shape with volume V and surface area S. For spherical particles, the calculation by formula (6) gives a value somewhat greater than the radius, particularly $l_{\text{eff}} = 4a/3$. For anisotropic particles such as nanorods, formula (6) gives a scalar estimate rather than the naturally expected tensor value, which takes into account the scattering anisotropy of electrons moving along and across the symmetry axis of the rod. Uskov *et al.*[65] proposed quantum mechanical model in which the surface scattering coefficient for spheroidal particles depends on the field direction and has different values for the transverse and longitudinal orientation of the field. The particle shape effect in the PR broadening was also studied in earlier publications.[66, 67] Note that Eqn (6) is more or less justified for smooth-shaped particles, but not for nanostars in which the core and spikes have different size and shape anisotropy. Khlebtsov *et al.*[68] proposed a two-component model of the dielectric function of nanostars. According to this model, the size correction to the bulk functions $\varepsilon_{\text{b}}(\omega)$ is carried out separately for the core and for the spikes considering the effective mean free paths of electrons in these parts.

The light absorption and scattering by a small particle are determined by the electrostatic polarizability [$\alpha(\omega)$] of the particle, which is calculated using the optical dielectric function $\varepsilon(\omega)$. For a sphere with small radius a in a uniform dielectric medium with the dielectric permittivity ε_{m}, the electrostatic polarizability is given by

$$\alpha = \frac{3V}{4\pi} \frac{\varepsilon - \varepsilon_{\text{m}}}{\varepsilon + 2\varepsilon_{\text{m}}} = a^3 \frac{\varepsilon - \varepsilon_{\text{m}}}{\varepsilon + 2\varepsilon_{\text{m}}} \qquad (7)$$

The extinction (C_{ext}), absorption (C_{abs}) and scattering (C_{sca}) cross-sections for a small sphere in the dipole approximation are related as [32]

$$C_{ext} = C_{abs} + C_{sca} = \frac{12\pi k}{a^3}\,\frac{\varepsilon_m \mathrm{Im}(\varepsilon)}{|\varepsilon-\varepsilon_m|^2}\,|\alpha|^2 + \frac{8\pi}{3}\,k^4|\alpha|^2 \qquad (8)$$

where $k = 2\pi n_m/\lambda$ is the wavenumber in an environment with the refractive index $n_m = \sqrt{\varepsilon_m}$; λ is the light wavelength in vacuum; $\varepsilon = \varepsilon(\omega) \equiv \varepsilon_p(\omega)$.

Equations (7) and (8) predict the localized PR for the polarizability and for integral optical cross-sections provided that

$$\varepsilon(\omega_{PR}) = \varepsilon(\lambda_{PR}) = -2\varepsilon_m \qquad (9)$$

Although the resonance condition (9) is determined by the real part of the dielectric function, the resonance absorption cross-section is limited, according to relation (8), by the value of the imaginary part. Combining the condition of resonance (9) with the Drude formula gives the following relation for the resonant angular frequency ω_{PR} and the resonance wavelength $\lambda_{PR} = 2\pi c/\omega_{PR}$ (c is the speed of light in vacuum) of a spherical particle

$$\omega_{PR} = \frac{\omega_p}{\sqrt{\varepsilon_{ib} + 2\varepsilon_m}} \qquad (10a)$$

$$\lambda_{PR} = \lambda_p\sqrt{\varepsilon_{ib} + 2\varepsilon_m} \qquad (10b)$$

where $\lambda_p = 2\pi c/\omega_p$ is the plasma oscillation wavelength,[32] the parameter ε_{ib} reflecting the contribution of interband transitions to the dielectric function of bulk gold is $\sim$12. Equation (10a) defines the first dipole resonance in a small sphere. As the particle size increases, multipole oscillations and the corresponding multipole plasmon resonances are excited. Mathematically, the latter correspond to the resonance frequencies for the partial coefficients a_n and b_n of the Mie theory [27]

$$\omega_n = \omega_p\left(\varepsilon_{ib} + \varepsilon_m\frac{n+1}{n}\right)^{-1/2} \qquad (11)$$

For understanding the physics of plasmon resonances, it is important to distinguish between two possible mechanisms of excitation of higher resonances. One mechanism applies to small-size particles with a large surface curvature and pronounced roughness or to contacts in the particle clusters. The induced charge distribution in these structures in resonance is highly non-uniform and does not correspond to the dipole approximation. Because of non-dipole charge distribution, higher multipoles are generated, despite the fact that the size of the system is generally markedly smaller than the incident light wavelength. Well-known examples of these objects are small cubic particles [69] or two nearly contacting small spheres.[70, 71]

The second mechanism corresponds to the excitation of multipole modes with increasing particle size where quasi-static regime switches to radiative regime. For example, for spherical particles $>100-200$ nm in diameter, it is necessary to take into account contributions of the higher coefficients of the Mie theory, which correspond to multipole modes.[27] In a first approximation, radiative damping for moderate-size particles can be taken into account by replacing electrostatic polarizability α [see Eqn (7)] with modified polarizability [32]

$$\alpha_R = \frac{\alpha}{1 + \varphi(ka)a^{-3}\alpha} \qquad (12)$$

$$\varphi(ka) = 2 + 2(\mathrm{i}ka - 1)\exp(\mathrm{i}ka) \simeq -(ka)^2 - \mathrm{i}\frac{2}{3}(ka)^3 \qquad (13)$$

In the small particle limit, Eqns (12) and (13) give the known result for the dynamic correction of polarizability [72, 73]

$$\alpha_R = a^3\frac{\varepsilon-\varepsilon_m}{\varepsilon + 2\varepsilon_m - \mathrm{i}(2/3)(ka)^3(\varepsilon-\varepsilon_m)} \qquad (14)$$

The plasmon optics of spherical gold particles has been described in detail in the literature;[32] therefore, we do not discuss it here and do not present absorption and scattering spectra. For our purpose, it is important that size tuning of the plasmon resonance is fairly weak and usually covers a narrow spectral range from 520 to 560 nm. This fact can be expressed quantitatively by modification of Eqn (10b) for the resonance wavelength [74]

$$\lambda_{PR} = \lambda_p\left[\varepsilon_{ib} + 2\,\varepsilon_m\varphi_0(x)\right]^{1/2} \qquad (15)$$

$$\varphi_0(x) = 1 + \frac{12x^2}{10}\left[1 + \frac{(\varepsilon''/\varepsilon_m)^2}{24}\right] + \frac{x^3}{3}\,\frac{\varepsilon''}{\varepsilon_m} \qquad (16)$$

$x = ka = 2\pi n_m a/\lambda$, $\varepsilon'' = \mathrm{Im}(\varepsilon)$. It can be seen from these relations that if $x < 0.5$, then size correction (16) to electrostatic approximation (15) can be replaced by unity. From the applied standpoint, PR of spherical particles taking place in the green-orange spectral range restricts the applicability of particles as optical biological labels, as the PR region overlaps with the absorption band of biological fluids (blood) of living organisms and is located away from the first transparency window of biological tissues.[75]

A radical improvement of PR tuning is attained when spherical particles are replaced by rods. For the understanding of principles of this tuning, it is convenient to consider a prolate particle as a spheroid with semi-axes (a,b,b); for this case, a simple solution is known for the electrostatic polarizability along the axes of symmetry [27]

$$\alpha_{a,b} = \frac{V}{4\pi}\,\frac{\varepsilon-\varepsilon_m}{\varepsilon_m + (\varepsilon-\varepsilon_m)L_{a,b}} \qquad (17)$$

where depolarization factors $L_{a,b}$ meet the condition $L_a + 2L_b = 1$. Unlike spherical particles, in the case of spheroidal particles, dipole approximation (17) predicts the excitation of two PRs corresponding to particle polarizability along and across the longer axis. The transverse resonance of gold nanorods in water occurs near 500 nm, and the longitudinal PR is easily tuned in the range from 500 nm to IR region by varying the aspect ratio. This is described by the relation

$$\lambda_{PR,a} = \lambda_p\sqrt{\varepsilon_{ib} + \left(\frac{1}{L_a} - 1\right)\varepsilon_m} \qquad (18)$$

which is derived from Eqn (17) by analogy with derivation of (10b). When the aspect ratio increases, the depolarization

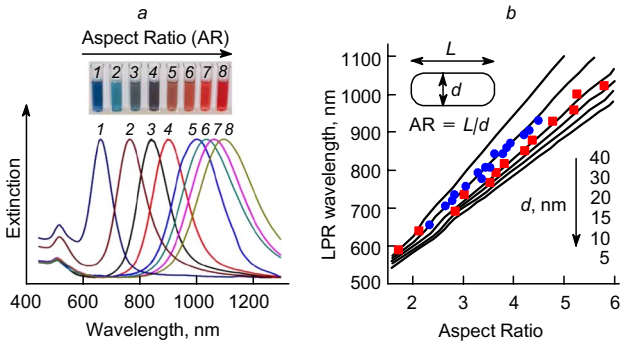


Figure 3. (*a*) Experimental extinction spectra of Au nanorods with aspect ratio of 2.31 (*1*), 3.35 (*2*), 3.96 (*3*), 4.65 (*4*), 5.52 (*5*), 5.90 (*6*), 6.20 (*7*), 6.55 (*8*).[76] (*b*) Localized PR wavelength as a function of the aspect ratio of cigar-like GNPs of 5 to 40 nm in diameter randomly oriented in water. Blue and red dots are experimental data obtained by etching (decrease in the length) of thick (26 nm) and thin (13 nm) rods, respectively.[76]

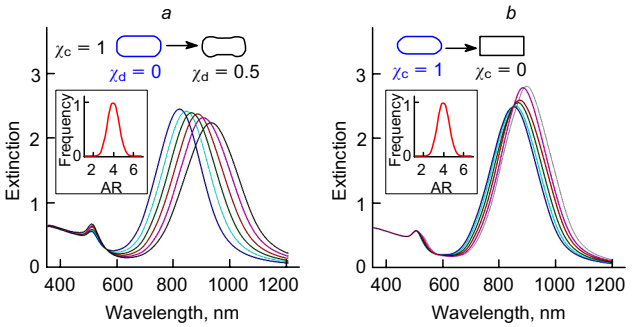


Figure 4. Change in the extinction spectra of Au nanorods with an average length of 40 (*a*) and 80 nm (*b*) randomly oriented in water upon the change in their shape. T-matrix calculation for the normal aspect ratio distribution of Au nanorods with a relative width of 0.3 (see insets). The average constant aspect ratio is 4 and gold concentration is 57 μg mL^{-1}. The Figures reflect the shift of the spectra to longer wavelengths upon a decrease in the central part diameter of the rods (*a*) and upon transformation of the cigar-like shape into a right circular cylinder (*b*). The parameters χ_c and χ_d determine the tip curvature of the nanorod and the decrease in the central diameter relative to the tip diameter, respectively. For quantitative determination of the shape parameters χ_c and χ_d, see Ref. 81. Published with permission from ACS Publications.

factor L_a tends to zero and the longitudinal PR wavelength theoretically infinitely grows. Nanorods with aspect ratios from 2 to 7 are used most often; this approximately corresponds to PR tuning from 600 to 1100 nm (Fig. 3).

For rods of a small volume, the PR wavelength in the dipole approximation depends only on the aspect ratio. However, with increasing rod volume, PR depends also on the volume or (when the aspect ratio is specified) on the particle thickness. This is illustrated in Fig. 3*b* for the model of gold nanocigars randomly oriented in water; this model is most adequate for high-quality experimental samples. When the aspect ratio is invariable, an increase in the particle thickness results in increasing theoretical PR wavelength. The controlled etching technique, initially proposed by Liz-Marzán's group,[77] was described by Khanadeev *et al.*[78] It can be seen that the experimental data qualitatively confirm the theoretical conclusion that the PR wavelength decreases with decreasing particle thickness. To our knowledge, this was the first experimental demonstration of this effect for a large number (30) of samples.

Apart from the aspect ratio, a considerable role in the PR position is played by particle morphology. In particular, upon the replacement of the cigar-like shape by the dog-bone shape of particles,[79] PR shifts to long-wavelength (red) region of the electromagnetic spectrum; the PR position changes even upon the change in the tip shape of the cigar-like nanorods.[80] The role of these effects is depicted in Fig. 4. It should be emphasized that in the given example, the mean aspect ratio for all polydisperse particle ensembles of different morphology is constant and amounts to 4. A detailed discussion of the effect of particle morphology on PR position and relevant references can be found in a study by Khlebtsov *et al.*[81]

One more possibility of PR tuning is related to the structure and/or composition of the particle. Most often, in the former case, spherical symmetrical layered structures are used, with dielectric layers alternating with metal layers. Of practical value are gold nanoshells coated on silica spheres described in the pioneering studies of Halas research group.[82] In the latter case, PR is tuned by varying the composition of the metal alloy since metals, gold and silver, have different dielectric functions. For the simplest two-layer sphere model, the formula for the electrostatic polarizability is well known.[27] However, this formula is inconvenient for analysis of PR tuning, especially for the case of multilayer spheres.[83] It would be rational to have a formula like Eqn (7) with some effective mean dielectric function, which would provide an exact electrostatic solution for a sphere with an arbitrary number of layers. This problem was solved by Khlebtsov *et al.*[84] on the basis of dipole equivalence principle. In particular, the mean dielectic function of a two-layer particle (ε_{av}) is calculated using the formula

$$\varepsilon_{av} = \varepsilon_2 \frac{1 + 2f_{12}\alpha_{12}}{1 - f_{12}\alpha_{12}} \tag{19}$$

$$f_{12} = \frac{a_1^3}{a_2^3} \tag{20a}$$

$$\alpha_{12} = \frac{\varepsilon_1 - \varepsilon_2}{\varepsilon_1 + 2\varepsilon_2} \tag{20b}$$

where a_1 and a_2 are the radii of the core and the shell, and ε_1 and ε_2 are the corresponding dielectric functions. Then the exact solution for the polarizability is given by the same formula (7) with ε being replaced by ε_{av} and the sphere radius a being replaced by a_2. The replacement of ε by ε_{ev} in resonance condition (9) results in analogue of the formula for the PR wavelength

$$\lambda_{PR,i} = \lambda_p\left(\varepsilon_{ib} + \varphi_{s,i}\varepsilon_m\right)^{1/2}, \; i = 1, 2 \tag{21}$$

$$\varphi_{s,i} = \frac{1}{2}\left[p \pm \left(p^2 - \frac{\varepsilon_1}{\varepsilon_m}\right)^{1/2}\right] \tag{22}$$

$$p = \frac{\varepsilon_1}{\varepsilon_m}\left(\frac{3}{4f_g} - \frac{1}{2}\right) + \frac{3}{2f_g} - \frac{1}{2} \tag{23}$$

where the plus sign in Eqn (22) is taken for IR resonance with $i = 1$, while the second short-wavelength resonance for gold in water is low and can be neglected. In relation (23), f_g is the volume fraction of gold in the particle; for thin shells,

$$f_g = 1 - \frac{a_{core}^3}{a_g^3} \simeq \frac{3\Delta a}{a_g} \ll 1 \qquad (23a)$$

As f_g decreases, the factor $\varphi_{s,l}$ increases and PR theoretically tends to infinity. Therefore, PR can be tuned by varying the ratio of the gold shell thickness to the silicate core diameter. The dipole equivalence principle was summarized by Khlebtsov [74] for multilayer non-spherical particles. In this case, PR can be tuned very successfully by combining the structure and shape effects.[85]

Comparison of relations (10b), (18) and (21) shows that for the considered particles, the PR wavelength can be represented in the following general form:

$$\lambda_{PR} = \lambda_p \sqrt{\varepsilon_{ib} + \varphi_{PR}\varepsilon_m} \qquad (24)$$

where φ_{PR} is 2 for uniform spheres, $L_{a,b}^{-1} - 1$ for nanorods and $\varphi_{s,i}$ for metal nanoshells coated on a dielectric core. Note that the versatile mechanism of plasmonic tuning by changing the aspect ratio or the shell : core ratio is also valid, to a certain extent, for geometrically complex particles such as ellipsoidal nanoshells, nanostars and nanocages. In the case of nanostars, tuning is performed by varying the height to base ratio of the spikes, while for nanocages, this is done by varying the ratio of the edge thickness to the edge length.

The above consideration is limited to the plasmonic tuning of single particles. Yet another mechanism is related to the electromagnetic interactions of the particles, for example, in aggregates. Simple examples are a dimer of two plasmonic spheres [70] or a linear chain of spheres.[86] Figure 5 *a* shows a shift of PR in a linear chain composed of twenty 15-nanometre gold nanospheres following a decrease in the distance between them from 3 to 0.3 nm, which induces a PR shift from 520 to 750 nm. A similar effect for chains comprising ten such nanospheres coated by dielectric layers of various thickness is illustrated in Fig. 5 *b*. The two-layer spheres in the chain are in contact; therefore, as the shell thickness decreases, the plasmonic particles approach one another from 10 to 0.5 nm and PR shifts from 520 to 650 nm.

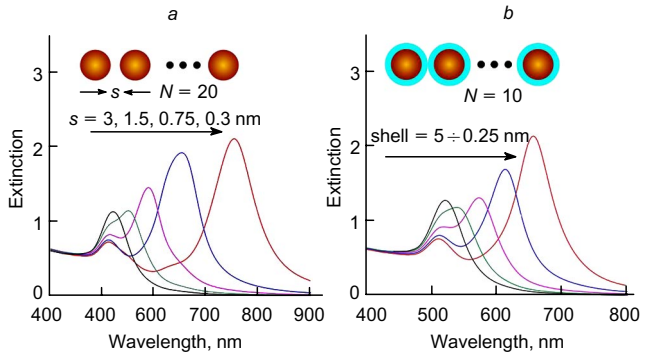


Figure 5. Evolution of the extinction spectra of linear chains consisting of twenty (*a*) and ten (*b*) 15-nanometre spherical GNPs. *a*: the distance between particles decreases from 3 to 0.3 nm. *b*: nanoparticles are coated by an insulator with a refractive index of 1.4; the particles are in contact; and the coating thickness decreases from 5 to 0.25 nm. The calculation was done by the authors of this review using the multiparticle T-matrix method for randomly oriented chains in water; the gold concentration was 57 mg mL^{-1}. Parameters of systems correspond to typical experimental conditions.

The shift of PR is correlated with subnanometre distances between the particles. This underlies the so-called plasmon ruler for dimers,[70, 87] for particles located near the gold surface,[88] and for particles in aggregates.[89] For an ensemble of particles interacting with a gold film surface, the size of the plasmonic gap can be precisely controlled by functionalization of the film with a molecular layer separating the nanoparticles from the metal surface. As the distance between the particle and the film decreases, the plasmon peak shifts to longer wavelengths by ~5 nm for every 1 Å of the distance between the surface and the nanoparticle.[88] Thus, each particle operates as a plasmon ruler for separatons ranging from 5 to 20 Å. The upper limit of the operating range was reported [88] to be 27 nm (Fig. 6). For nanoparticles in aggregates, the long-wavelength PR correlates with the distance between particles; hence, the extinction of aggregates can be used as a plasmon ruler.[89] However, the accuracy of this method cannot be high because of the dependence of the PR shift on the uncontrolled aggregate size and fractal structure. Discussion of the optical properties of metal clusters is beyond the scope of this review; references to publications on this subject can be found in Khlebtsov's publication.[74]

3. Methods for synthesis of large monodisperse gold nanospheres

For gold nanospheres of < 30 nm in size, the PR wavelength is ~ 520 nm. Pronounced shifts of PR to longer wavelengths (up to 800 nm) are observed only for larger GNPs. This Section addresses methods of synthesis and plasmon spectra of particularly such particles.‡ Methods used to prepare GNPs can be conventionally classified into two large groups.[12, 90–94] The first group includes dispersion methods based on the dispersion of metals. The second group comprises condensation methods in which nanoparticles of a reduced metal are formed from the ions of appropriate salts.

Among the condensation methods used to prepare gold nanospheres of 15–150 nm in size, citrate method is used most widely.[95] The synthesis of GNPs with sodium citrate

‡ Plasmon spectra of < 100 nm particles are considered in a review.[12]

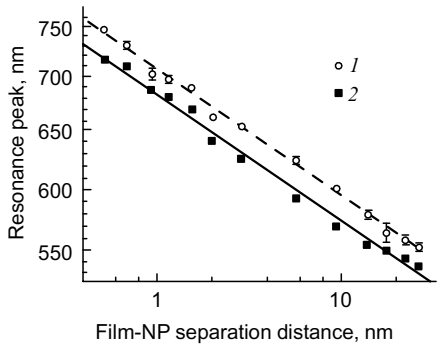


Figure 6. Shift of PR of nanoparticle/film samples depending on the thickness of the molecular spacer (from 5 Å to 27 nm) in the scattering (*1*) and extinction (*2*) spectra. The experimental data for aminothiol spacers were combined with data for polyelectrolyte layers and approximated by power functions like $y = y_0 x^{-n}$ (y_0 = 706.2, n = 0.0765, scattering; y_0 = 682.9, n = 0.0772, extinction).[88] Published with permission from ACS Publications.

as the reducing agent is called either the Turkevich method, or Frens method, or sometimes the Turkevich–Frens method.§

According to transmission and scanning electron microscopy (TEM and SEM, respectively), the spherical nanoparticles obtained by the citrate process are more shape- and size-uniform than the particles obtained using other reducing agents (white phosphorus, acetone, tannin, oxalic acid, hydroxylamine, carbon monoxide, acetylene, citric acid).[97]

According to the citrate method proposed by Frens,[98] a 1% aqueous solution of sodium citrate is added to a boiling 0.01% aqueous solution of $HAuCl_4$, with the amount of sodium citrate being varied depending on the desired particle size. Particularly, the adjustment of concentrations for the formation of particles with a specified size distinguishes this method from other methods in which sodium citrate is also used as a reducing agent. Using a constant amount of $HAuCl_4$ to prepare 50 mL of GNPs, Frens added 1.0, 0.75, 0.5, 0.3, 0.21 and 0.16 mL of a 1% solution of sodium citrate (the molar ratio of the reactants decreased from 2.7 to 0.4; the average diameter of the resulting GNPs was 16, 24.5, 41, 71.5, 97.5 and 147 nm, respectively). After formation of a sol ($\sim$15 min), the addition of fresh portions of the reducing agent did not result in noticeable optical changes. The maximum absorbance of the obtained sols varied in the 0.8–1.2 range, and the concentration of gold was constant and amounted to 57 μg mL^{-1} (2.9×10^{-4} mol L^{-1}). A change (increase or decrease) in the $AuCl_4^-$ to citrate molar ratio outside the optimal range (0.75–1.35) led to lower reaction rate and greater diameter of the particles.[99]

The possible control parameters for the citrate synthesis are the ratio of the $AuCl_4^-$ and citrate concentrations,[100, 101] pH of the reaction mixture, temperature, reaction duration and the order of addition of the reactants.[102, 103]

The main drawback of the citrate method is the shape non-uniformity of large (>50 nm) GNPs. The shape of such particles is not spherical; they differ in size, and gold sols are unstable during storage. To date, quite a few varieties of the classical citrate synthesis of GNPs have been proposed; they are mainly directed towards extension of the range of sizes and preparation of nanoparticles identical in size in shape. As a rule, this is attained by introducing additional compounds, which improve characteristics of the target nanoparticles, by varying pH and temperature, and by using physical methods to initiate the synthesis. The most promising approaches that allow the synthesis of large monodisperse spherical GNPs are considered below.

The use of UV irradiation instead of heating for the citrate synthesis of GNPs results in the formation of large spherically shaped particles.[104] A similar result was attained by adding traces of the Ag^+ ions in the reaction mixture.[105]

In some versions of the citrate synthesis, pre-synthesized seeds were first added to the reaction medium and then they served as condensation centres.[106] According to published data,[52, 107] the large particles thus formed with a diameter of 50–300 nm (Fig. 7) had a much narrower size distribution than similar particles obtained by other methods.

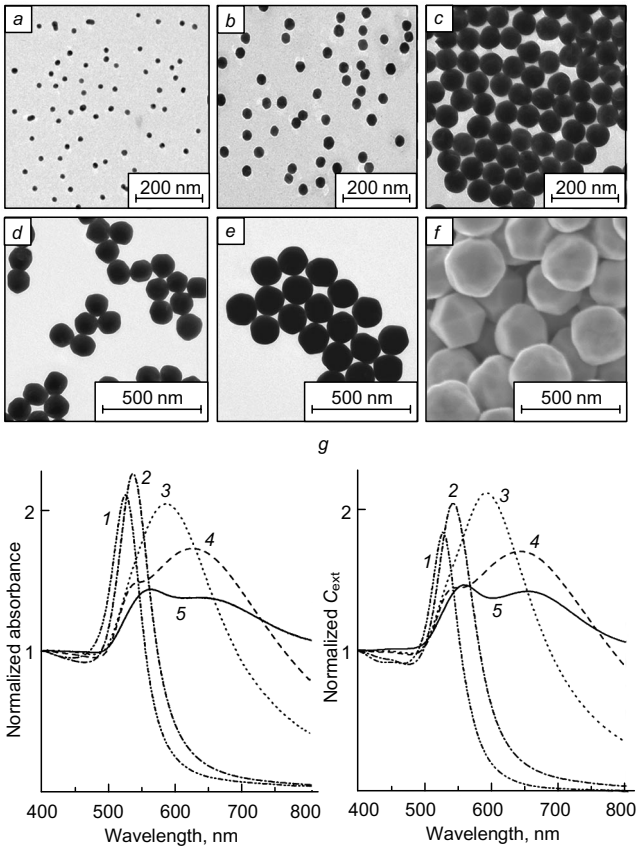


Figure 7. TEM images of GNPs of sizes: 15 ± 2 (seeds) (*a*), 31 ± 3 (*b*), 69 ± 3 (*c*), 121 ± 10 (*d*), 151 ± 8 nm (*e*); SEM image of GNPs of 294 ± 17 nm size (*f*). (*g*) experimental normalized extinction spectra¶ (on the left) and calculated normalized extinction cross-section spectra (on the right) for GNPs of sizes 30 (*1*), 69 (*2*), 118 (*3*), 150 (*4*), 294 nm (*5*) (normalization was done to the value for 400 nm).[52] Published with permission from ACS Publications.

The key requirement to the reaction conditions needed to obtain isodisperse and isomorphic sols is to preventi the formation of new seeds. As a rule, this is attained by gradual increase in the gold concentration in a medium containing mature particles of metal sol, and by control over temperature and pH.[107, 108] Apart from sodium citrate, other reducing agents can be used such as ascorbic acid,[107, 109] hydroquinone,[51, 110] hydrogen peroxide,[111] tris(hydroxymethyl)aminomethanes[112] or hydroxylamine.[113]

Uniform single crystalline gold nanospheres of 5–150 nm in diameter were synthesized by the seed-based method in a medium containing cetyltrimethylammonium chloride (CTAC) micelles with ascorbic acid being used as the reducing agent.[54] The diameter of the obtained nanospheres can be exactly controlled by varying the size and/or number of seeds. The high quality of nanoparticles obtained by this method is illustrated by Fig. 8. A drawback of this method is increasing time of the synthesis (1 h) for particles of >15 nm in diameter, since the rate of addition of $HAuCl_4$ with a syringe pump is

§ This method should rightly be called after Borovskaya, because D.P.Borovskaya was the first who proposed in 1934 to use sodium citrate as the reducing agent to obtain colloidal gold;[96] meanwhile, the paper by John Turkevich *et al.*[97] was published in 1951, and the publication by Frens[98] appeared in 1973.

¶ Here and in Fig. 13, the vertical axis is designated as absorbance to follow the original publications; however, the authors measured the attenuation using a conventional spectrophotometer, *i.e.*, actually they measured the extinction.

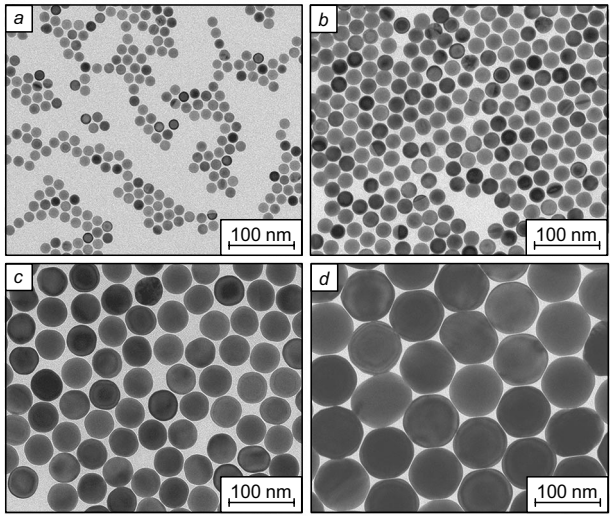


Figure 8. TEM images of single-crystalline Au nanospheres with controlled diameters of 15 (*a*), 23 (*b*), 46 (*c*), 80 nm (*d*).[54] Published with permission from Wiley.

2 mL h^{-1}. The experimental and simulated UV/Vis extinction spectra of Au nanospheres of various diameters reported by Zheng *et al.*[54] had similar shapes and positions of extinction peaks. Since the simulation was performed with the assumption of ideally spherical single particles, comparison of the experimental and theoretical spectra suggests that the prepared GNPs were spherical (see Fig. 8).

Ruan *et al.*[114] proposed a seed-based method in combination with mild oxidation for the synthesis of GNPs of 20–220 nm in diameter. The mild oxidation of seeds took place in the presence of $HAuCl_4$ and cetyltrimethylammonium bromide (CTAB). The samples had a spherical shape, smooth surface and narrow size distribution with relative standard deviations of 4–8% (Fig. 9). The authors showed that the size of final GNPs depended on the added amount of small seeds, with their growth and oxidation conditions being the same. For particles of diameters 54 ± 2, 69 ± 3, 88 ± 4, 103 ± 6, 137 ± 9, 177 ± 14 and 221 ± 16 nm, the volumes of added seeds were 4, 2, 1, 0.5, 0.25, 0.125 and 0.0625 mL, respectively. The amounts of $HAuCl_4$ and CTAB remained invariable.

The resulting nanoparticles were stable in water and retained the spherical shape for long periods of time (more than 6 months). Afterwards, larger GNPs precipitated. Shaking or sonication induced repeated dispersion without formation of aggregates. The colour of GNP samples was different, ranging from red to purple or yellow. As the average particle diameter increased from 24 to 221 nm, the PR peaks gradually shifted to the red region of the electromagnetic spectrum: from 521 to 806 nm. In the case of larger GNPs, peak broadening was observed. In the extinction spectra of the samples with average diameters of 177 and 221 nm, quadrupole plasmon modes appeared at 547 and 565 nm, respectively. The experimental extinction spectra were in good agreement with the spectra calculated by the Mie theory (Fig. 10).

In 2021, Zhang *et al.*[55] proposed one-step polyol synthesis of the monodisperse single-crystalline Au nanospheres with ultrasmooth surface and tunable size from 30 to 100 nm. The nanoparticles were synthesized using aqueous solutions of $HAuCl_4$, poly(diallyldimethylammonium chloride) (PDDA), $AgNO_3$ and HCl. The synthesis was conducted in ethylene glycol. The final concentrations of $HAuCl_4$, PDDA and $AgNO_3$ in the solution were 0.5, 25 and 0.01 mmol L^{-1}, respectively. The mixture was vigorously stirred at room temperature for uniform distribution of reactants. Then the freshly prepared solution of the mixture was heated in an oil bath at 220 °C for 2 h. After this period, the colour of the solution changed from yellow to red. The final products were collected by centrifuging and washed many times with deionized water to remove the residual amounts of ethylene glycol and PDDA. TEM and SEM images of the obtained GNPs are depicted in Fig. 11.

During the synthesis, Au nanospheres underwent a unique change in the morphology from octahedral to spherical as a result of selective etching of the surface with the dissolved $O_2 + Cl^-$ (Cl^- anion from $HAuCl_4$, HCl, PDDA) and dynamically tailored growth direction for silver ions. Using this protocol, it is possible to perform a large-scale synthesis (> 500 mL in one experiment) of Au nanospheres stable due to the isotropic surface tension (they were stored in ethylene glycol for more than two years).

The initial reaction solution in this synthesis contains a sufficient amount of $O_2 + Cl^-$ pairs; owing to their pro-

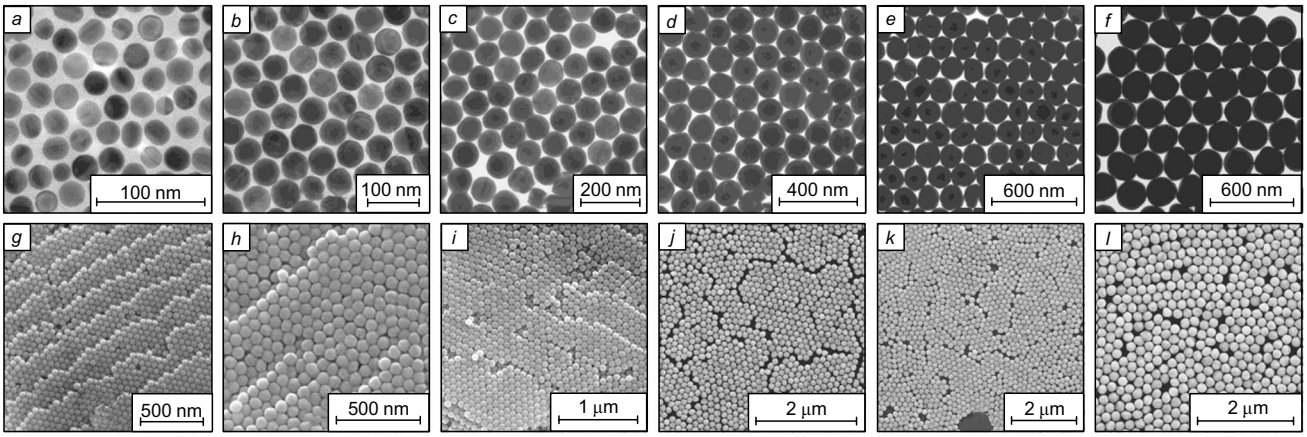


Figure 9. TEM (*a*–*f*) and SEM images (*g*–*l*) of Au nanospheres of diameters 24 ± 2 (*a*), 54 ± 2 (*b*), 88 ± 4 (*c*), 137 ± 9 (*d*), 177 ± 14 (*e*), 221 ± 16 (*f*), 54 ± 2 (*g*), 69 ± 3 (*h*), 88 ± 4 (*i*), 137 ± 9 (*j*), 177 ± 14 (*k*), 221 ± 16 (*l*).[114] Published with permission from Wiley.

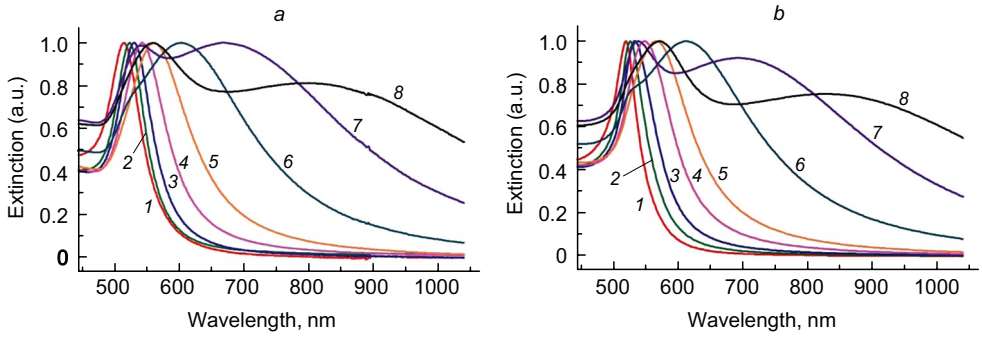


Figure 10. Normalized experimental (measured on a spectrophotometer) (*a*) and calculated (by the Mie theory) (*b*) extinction spectra of GNP samples. The samples were GNP colloids with average diameters of 24 ± 2 (*1*), 54 ± 2 (*2*), 69 ± 3 (*3*), 88 ± 4 (*4*), 103 ± 6 (*5*), 137 ± 9 (*6*), 177 ± 14 (*7*), 221 ± 16 nm (*8*).[114] Published with permission from Wiley.

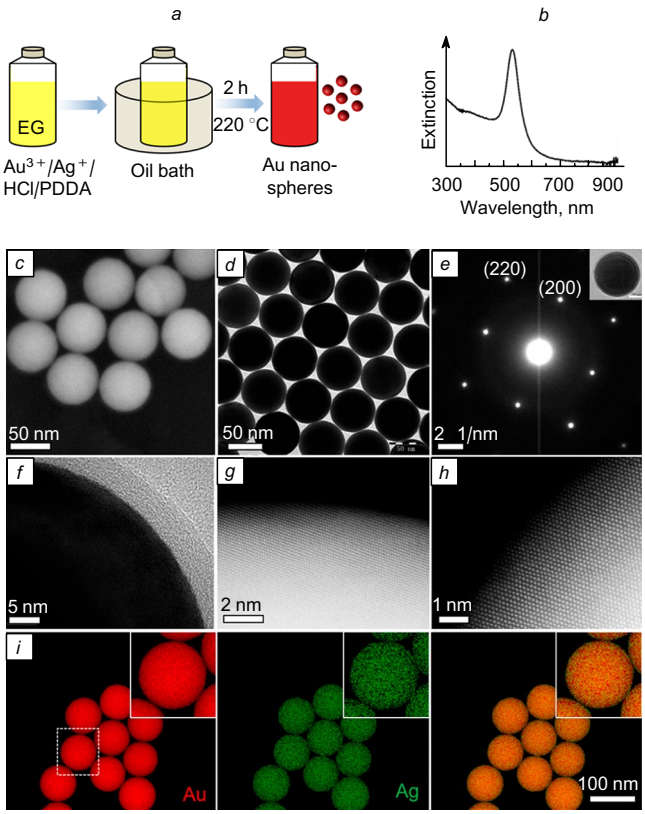


Figure 11. Scheme of the synthesis, morphology and structural characteristics of Au nanospheres. (*a*) Preparation of GNPs; (*b*) extinction spectrum of the colloid; (*c*) field-emission SEM image; (*d*) TEM image; (*e*) selected area electron diffraction; the inset shows the TEM image of a single GNP; (*f*) high-resolution TEM image; (*g*, *h*) high-angle annular dark-field scanning TEM images; (*i*) high-resolution EDS maps of element distribution: the left panel shows the distribution of gold atoms (99.4%), the middle panel shows the distribution of silver atoms (0.6%), and the right panel is superposition of both distributions; the insets in the upper right corners are enlarged selected area images. The gold mapping contrast is more intense at the centre and less intense at the periphery; the silver atoms are distributed uniformly. Thus, the structure can be characterized as Au(core)/Ag(nanoshell).[55] Published with permission from ACS Publications.

nounced capacity for the oxidative etching, all structural defects of gold nanoparticles are removed, and high-purity single crystalline products are formed in an early stage. Since the particles have an ideal spherical shape and uniform size, the PR wavelengths of Au nanospheres of various sizes are in good agreement with theoretical predictions (Fig. 12).

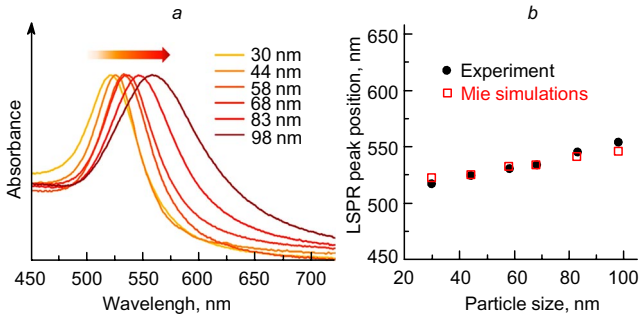


Figure 12. Extinction spectra of Au nanospheres (*a*) and localized PR peak position *vs.* particle size found experimentally and by modelling in terms of Mie theory (*b*).[55] Published with permission from ACS Publications.

Do *et al.*[53] also reported a method of seeded growth of uniform smooth spherical GNPs with a narrow size distribution. Gold nanoparticles of up to 220 nm in size were obtained using formaldehyde as a reducing agent in the absence of a stabilizer in an aqueous solution at room temperature. Seeds of 1–3 nm in diameter were synthesized by reduction of $HAuCl_4$ with tetrakis(hydroxymethyl) phosphonium chloride. These seeds were dispersed in the growth solution at pH 9.0 in the presence of formaldehyde. The seeded growth was multistep; therefore, by controlling the ratio of $HAuCl_4$ and seeds, it was possible to precisely control the GNP size. The resulting Au nanospheres were characterized by TEM, dynamic light scattering and UV/Vis absorption spectroscopy. The method is perfectly reproducible and can considerably improve the monodispersity of nanospheres.

Flow reactors for the controlled scalable synthesis of Au nanospheres with a size of up to 150 nm were proposed,[115] and methods for the preparation of micrometre-size gold particles were developed.[116, 117] Particles of this type are convenient tools to be used in SERS-based methods.

The key procedures for the synthesis of large GNPs are characterized in Table 1.

The fundamentals of the synthesis of large gold nanoparticles considered in this Section form the basis for understanding of the mechanism of formation of both Au nanospheres and other nanoparticles with precisely controlled size and shape.

4. Synthesis and optical tuning of gold nanorods

The crystal structure features of gold salts makes the formation of Au nanorods upon the reduction of Au salts in solution statistically unlikely; therefore, the nano-

Table 1. Key procedures for the synthesis of large Au nanospheres.

GNP size, nm	Reducing agent	Synthesis details	Ref.
50 – 300	Sodium citrate	Seed-based method in water	52, 107
5 – 150	Ascorbic acid	Seed-based method in the presence of CTAC	54
20 – 220	Ascorbic acid	Seed-based method in the presence of CTAB	114
30 – 100	Ethylene glycol	Polyol synthesis in ethylene glycol in the presence of PDDA, $AgNO_3$ and HCl on an oil bath at 220 °C	55
25 – 220	Formaldehyde	Seed-based method in water	53

rods are synthesized using anisotropic templates. The first method based on the electrochemical deposition of gold inside the nanopores of polycarbonate or aluminium membranes was proposed by Martin.[118] Initially, this method was used to modify microscopic electrodes, but later it was applied to prepare nanocomposites and colloids of Au nanorods.[119] The diameter of the resulting nanoparticles corresponds to the pore diameter of the membranes, which provides for the formation of equally thick particles,[120] while their length and plasmon resonance can be precisely controlled by varying the amount of the deposited metal. A drawback of using rigid templates is that the method cannot be scaled.

A higher yield of Au nanorods can be obtained by using the method proposed by Wang's group,[121] which is based on the electrochemical formation of metal clusters in reverse micelles. However, due to poor reproducibility and sophisticated influence of various factors, the original protocol using CTAB has not found use in the modern experimental practice.[122]

A considerable progress was attained after publication by Murphy and co-workers,[123] who proposed a new type of the synthesis, namely, seed-induced growth of Au nanorods in solutions of cationic surfactant. According to the synthetic protocol, solutions of CTAB, $HAuCl_4$, ascorbic acid and a minor amount of small (3 nm size) gold nanoparticles were mixed in a flask. This gave rise to Au nanorods with an average thickness of 15 nm and an aspect ratio of ~4.5. Longer particles were obtained using a three-stage procedure. Apart from nanorods, particles of various shapes (spheres, cubes, prisms, *etc*.) were formed in solution. Initially, the yield of Au nanorods did not exceed 4%, but according to a modified protocol reported later,[124] high yields of nanorods (up to 90%) were attained owing to optimization of pH of the growth solution.

The mechanism of formation of Au nanorods in solutions of cationic surfactants was studied by quite a few research groups.[125–128] State-of-the-art data and relevant references can be found in the publication by Park *et al*.[16] The growth of Au nanorods includes the following stages:

— isotropic growth of small seeds with a bimodal distribution;

— anisotropic growth of twinned seeds with enriched {100} and {111} crystal faces;

— further growth of Au nanorods between the {111} and {100}/{110} faces, giving rise to dumb-bells;

— final formation of cigar-like nanorods.

In all four stages, the crucial role is played by CTAB molecules and silver ions. For details, see a paper[117] and a review.[17]

A real breakthrough in synthesis of Au nanorods was made in 2003 by Nikoobakht and El-Sayed,[125] who proposed two key improvements:

— the use of gold nanoclusters stabilized by CTAB as seeds,

— the addition of silver nitrate to the growth solution.

Using this protocol, high-quality ~15 nm-thick particles with a length from 30 to 70 nm were obtained in high yields (up to 90%).

Typical TEM images of Au nanorods, prepared as proposed by Nikoobakht and El-Sayed,[125] are shown in Fig. 13 *a*. According to this method, the concentrations of silver and seeds are critically important for the precise control over the aspect ratio and plasmon resonance (Fig. 13 *b*,*c*). After the first publication,[125] the Nikoobakht and El-Sayed method was modified by many researchers. In addition, the effects of the concentrations of gold, additional surfactants, salts and acids were studied. Currently, numerous reviews considering in detail the methods for the synthesis of Au nanorods are available.☆

The above-described method[125] is the gold standard in the synthesis of Au nanorods; it is successfully used in laboratories of various countries, although it is not free from drawbacks such as

— PR tuning is limited to 900 nm wavelength, and the greatest aspect ratio for Au nanorods is usually < 5;

— it is impossible to prepare relatively thick (> 20 nm) or thin (< 10 nm) nanorods;

— the yield of the target particles obtained by optimized protocols is ~90%, *i.e*., the colloids of Au nanorods contain ~10% impurities.

A solution to the two first-mentioned problems was found in 2013 by researchers of Murray's group,[128] who proposed a method for the synthesis of Au nanorods using binary surfactant mixtures. The reaction rate was lower compared to that in the method of Nikoobakht and El-Sayed; this markedly extended the possibility of tuning of the PR wavelength and nanorod size (Fig. 13 *d*,*e*). In particular, it became possible to synthesize particles with a thickness of 12 to 100 nm with an aspect ratio of 2 to 10. The Murray method covers the whole range of PR wavelengths of interest: 600 to 1300 nm. An additional advantage of this method is a low amount of impurities in the final product.

A significant modification of the Nikoobakht and El-Sayed method was proposed by Vigderman and Zubarev,[129] who used hydroquinone as a reducing agent for gold ions. According to their protocol, it is possible to obtain long Au nanorods with plasmon resonance at > 1200 nm wavelength (Fig. 13 *f*).

The authors of the above-mentioned papers successfully solved the problem of synthesis of relatively large nanoparticles; however, the developed methods did not allow the preparation of small Au nanorods of < 10 thickness.

☆ We advise to pay primary attention to the paper by Scarabelli *et al*.,[126] who summarized the techniques and addressed important details of the synthesis of high-quality Au nanorods.

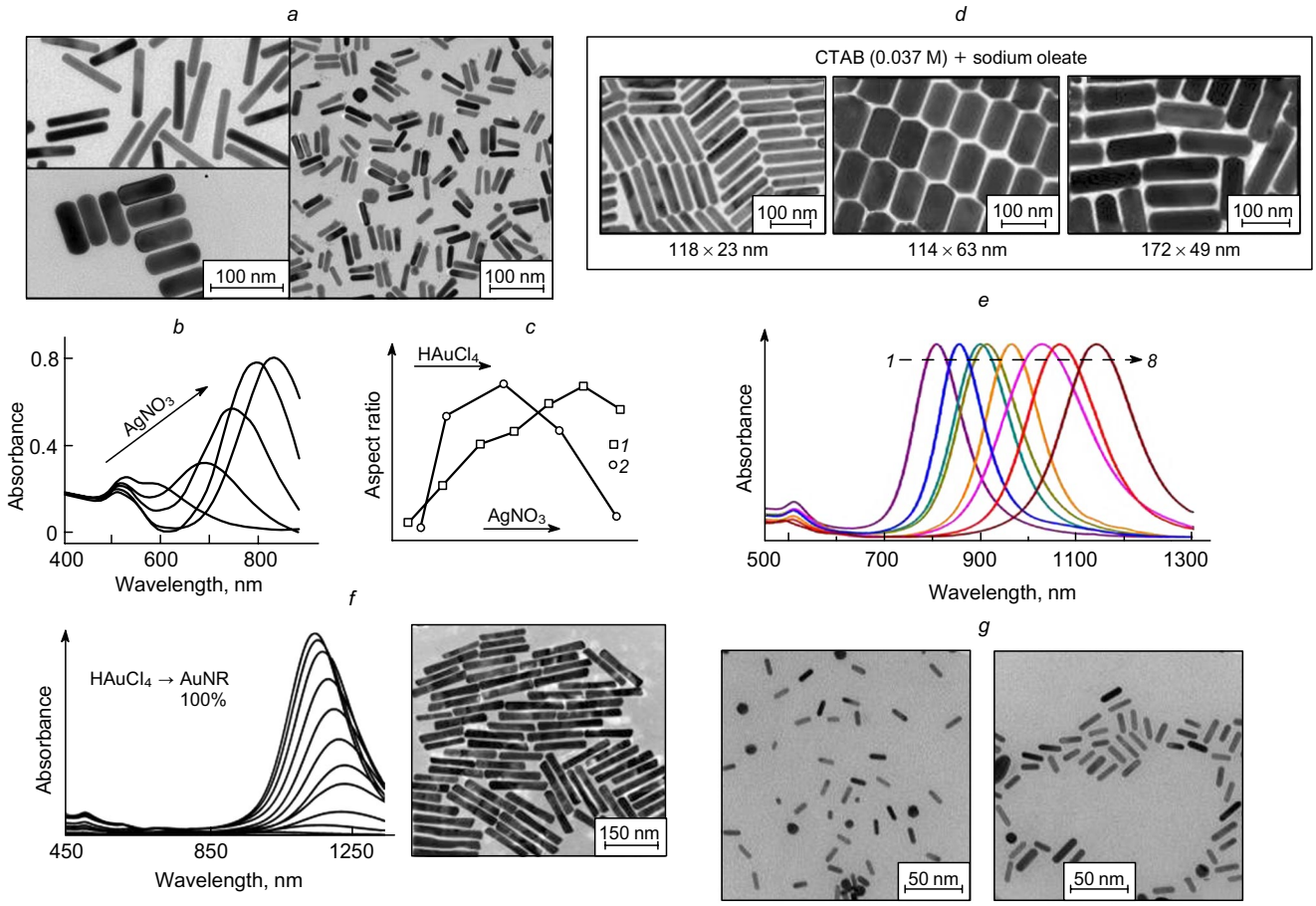


Figure 13. (*a*) TEM image of Au nanorods synthesized by the protocol reported in Ref. 125. (*b*) Absorption spectra of Au nanorods synthesized with increased amount of silver nitrate.[125] (*c*) Aspect ratio *vs.* silver (*1*) and gold (*2*) concentrations in the growth solution.[125] (*d*, *e*) TEM images and absorption (extinction) spectra measured in the synthesis of Au nanorods in a binary surfactant mixture;[128] the nanorod dimensions (length × thickness, nm) for spectra 1 to 8 were 88 × 23 (*1*), 99 × 23, 96 × 21, 89 × 17, 111 × 21, 130 × 22, 102 × 16, 128 × 17 (8). (*f*) Kinetics of the absorption (extinction) spectra and TEM images of Au nanorods synthesized with hydroquinone as the reducing agent; the method ensures 100% (in relation to gold) conversion of $HAuCl_4$ to Au nanorods (AuNR).[129] (*g*) TEM images of Au nanorods obtained by the seedless method. Figure a was created by the authors using published data;[13,81] Figs *b*–*f* are published with permission from ACS Publications; Fig. *g* courtesy of Salavatov *et al.*[127] taken from their research archive.

Indeed, the most obvious way to reduce the size of final particles is to increase the number of seeds, but in the presence of too many seeds, the yield of Au nanorods markedly decreases. In order to solve this problem, several research groups [127,130,131] proposed a seedless growth technique. In a typical synthesis, solutions containing CTAB, $HAuCl_4$, silver nitrate and ascorbic acid were mixed in a reaction flask. A sodium borohydride solution was added to initiate the growth of nanorods. For ensuring the monodispersity of nanoparticles, it is necessary to adjust pH and $NaBH_4$ concentration.†† This may give <5 nm thick Au nanorods with a length from 15 to 25 nm depending on the concentration of the reactants (Fig. 13 *g*).

According to all protocols mentioned above, the aspect ratio and plasmon resonance of Au nanorods are controlled by varying the reactant concentrations and pH of the growth solution; this leads to a limited reproducibility of the synthesis. In particular, the PR wavelength can be reproduced with an accuracy of at best $\sim$20 nm. Therefore, a different strategy is required for finer tuning of PR to the desired wavelength with an accuracy of, for example, 1–5 nm.

Relatively recently, two protocols have been proposed for exact tuning of the PR wavelength and volume of Au nanorods, which determines the absorption (scattering) coefficient. Tuning is based on a combination of overgrowth [132] and etching [77,78] processes (Fig. 14). During overgrowth, the total volume of the rod increases, while the PR wavelength and the aspect ratio decrease. Etching of the samples results in a gradual decrease in the PR wavelength. It is important that both protocols produce samples with very similar particle morphology and similar concentrations. Other methods that use independent synthesis to obtain a specified longitudinal PR wavelength do not produce equal particle concentrations in the samples. The PR tuning range is roughly the same for both processes: from the PR wavelength of the initial colloid to $\sim$600 nm. Owing to the possibility of complete control over the process of etching, the PR wavelength can be tuned with an unprecedented accuracy close to 1 nm. As an example,

†† Note that the addition of $NaBH_4$ to the reaction mixture immediately results in the formation of small gold nanoclusters, which serve as the condensation centres in the subsequent reduction of gold. Therefore, the term seedless is actually not entirely relevant. The seeds are still present in the beginning of the synthesis, but they are not prepared separately.

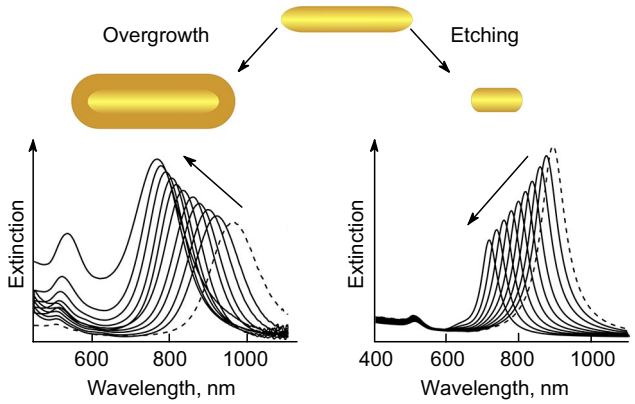


Figure 14. Evolution of the extinction spectra during overgrowth and etching processes of Au nanorods. The arrows show the direction of the evolution of the spectra starting from the spectrum of initial particles (shown by a dashed line).[76]

Fig. 15 shows data reported by Khlebtsov *et al.* [133] Comparison of measured (Fig. 15*f*) and simulated (Fig. 15*g*) spectra showed coincidence in the peak positions and intensity. Thus, the overgrowth and etching techniques can serve for rational design of nanorod geometry, including control over the aspect ratio and absorption (scattering) cross-sections. The key methods for obtaining Au nanorods with specified geometric and optical parameters are summarized in Table 2.

Irrespective of the process of synthesis, the final products always contain a certain amount of impurity particles (from 1 to 50% depending on the quality of the protocol). In the presence of spherical, cubic or triangular small impurity particles, the position of the longitudinal PR of nanorods does not change; however, another criterion, the intensity ratio between the long-wavelength and short-wavelength peaks, first proposed by Alekseeva *et al.*[134] and characterizing the GNP quality, decreases. This basically restricts the use of Au nanoparticles containing impurities, for example, for measurement of scattered light depolarization.[135] The most obvious way to remove impurity particles from colloids of Au nanorods is centrifugation.[136] If the sizes of Au nanorods and by-products are markedly different, the centrifugation parameters can be adjusted to ensure efficient separation (Fig. 16).

Unfortunately, the weights of nanorods and impurity particles are often quite similar; therefore, numerous centrifugation (purification) stages are required to remove the impurities. In practice, multi-stage separation leads to the loss of a greater part of the sample material. Khlebtsov *et al.*[135] proposed an improved technique for centrifugation. The key idea is to use a glycerol concentration gradient (Fig. 16*b*) for more efficient separation of nanoparticles of different shape and weight. Since complete precipitation of the particles is not required, primary attention is paid to the intermediate precipitation, in which several fractions (coloured bands) appeared in the separation tube, which indicated that the colloid has been split into fractions comprising different particles inside the tube. In a sense, the process was similar to thin layer chromatography. A drawback of this method was in the small volume of the sample, which precludes the preparative separation of even 100 mL of a colloid solution.

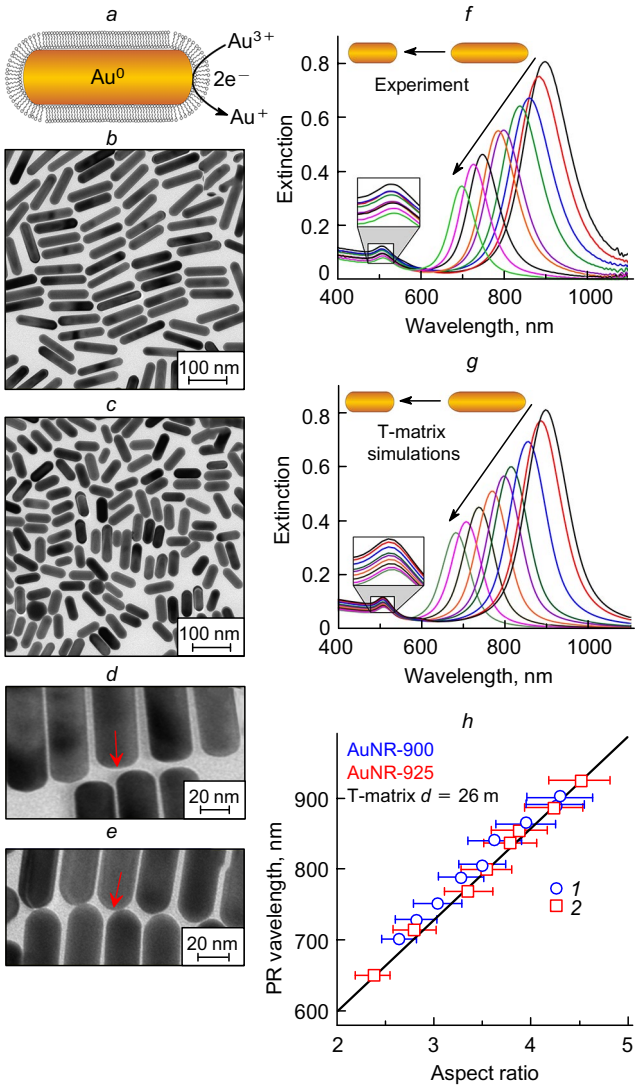


Figure 15. (*a*) Selective etching of Au nanorods. (*b*, *c*) TEM images of the initial and etched nanorods with longitudinal resonances at 900 and 700 nm, respectively. (*d*, *e*) TEM images of the flatter tips of the initial rods and rounded tips of slightly etched particles with a minimum amount of CTAB complexes. (*f*) Experimental extinction spectra obtained upon the addition of variable amounts of $HAuCl_4$. (*g*) Extinction spectra of cigar-like gold nanoparticles randomly oriented in water for a constant average thickness of 26 nm (TEM data) and variable average length derived from TEM images. The arrows in Fig. *f* and *g* show the direction of the evolution of the spectra upon sample etching. (*h*) Dependence of the position of longitudinal PR on the aspect ratio according to T-matrix calculation (line) and measurements for two independent sets of Au nanorod samples (AuNR-900 and AuNR-925) with initial plasmon resonances at 900 (*1*) and 925 nm (*2*); the standard deviations were obtained from the results of TEM analysis.[133] Published with permission from ACS Publication.

An interesting way of separation was proposed by Sharma *et al.*[137] When nanorods are centrifuged in a tube with a conical bottom, the target particles are mainly deposited on the wall, while impurities are concentrated on the tube bottom (Fig. 16*a*). Careful decanting of the supernatant significantly increases the concentration of nanorods, which suggests that the colloidal stability of nanoparticles depends on their shape. Actually, this assumption underlies the method for purification of Au-

Table 2. Key procedures for the synthesis of Au nanorods.

Essence of the method	Method for PR control	Aspect ratio	λ_{PR}, nm	Yield (%)	Drawbacks of the method	Ref.
Metal precipitation in membrane pores	Amount of precipitated metal	2.5 – 20	600 – 1700	~100	Low GNP concentration	118 – 120
Electrochemical synthesis in CTAB micelles	CTAB concentration	2.5 – 5	650 – 900	70	Poor reproducibility	121
Seed-based synthesis in CTAB micelles	Seed concentration	4.6 – 18	–	4	Low yield of GNPs, poor control over PR position	123
Seed-based synthesis in CTAB micelles	Seed concentration, pH	4.5 – 16	800 – 1600	90	Poor control over PR position	124
Seed-based synthesis in CTAB micelles in the presence of $AgNO_3$	Seed concentration, silver nitrate concentration	2 – 4.5	600 – 900	90	GNP thickness can only be in the 12 – 16 nm range	125
Seed-based synthesis in CTAB/sodium oleate micelles	Seed concentration, silver nitrate concentration	2 – 10	600 – 1400	~100	Impossibility of obtaining GNPs with a thickness < 12 nm	128
Seed-based synthesis in CTAB micelles using hydroquinone	Seed concentration, silver nitrate concentration	5 – 13	900 – 1700	95	Poor control over PR position	129
Seedless synthesis in CTAB micelles	Silver nitrate concentration	2 – 6	600 – 900	~80	Impossibility of obtaining GNPs with a thickness > 12 nm	127 – 131
Controlled overgrowth of Au-nanorods	Concentration of the initial Au nanorods	2 – 8	600 – 1100	~100	Necessity to use high-quality initial GNPs	132
Controlled etching of Au-nanorods	Concentration of $HAuCl_4$	2 – 8	600 – 1100	~100	Necessity to use high-quality initial GNPs	77, 78

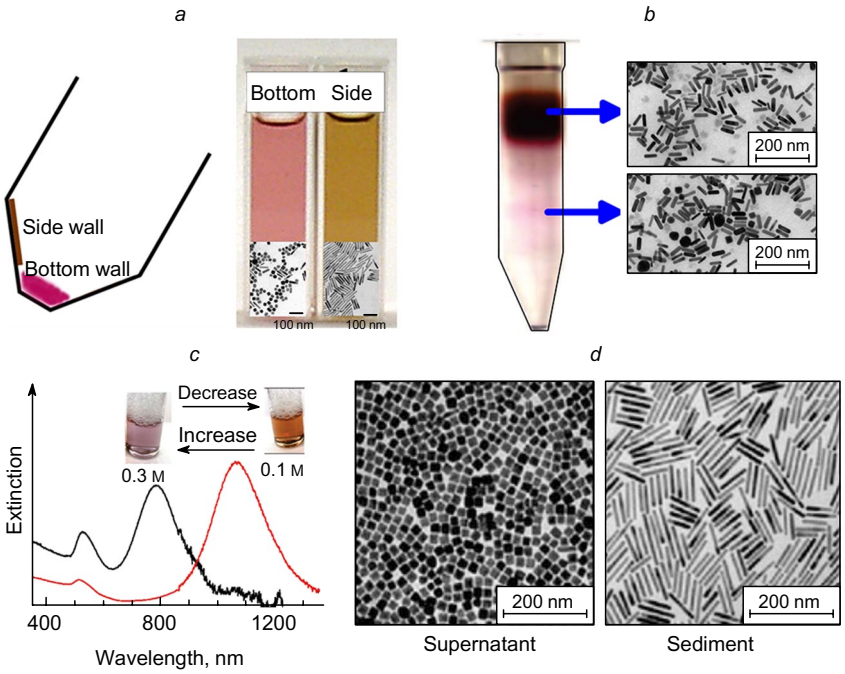


Figure 16. (*a*) Tube after centrifugation of a colloid of Au nanorods (on the left) and colour of the obtained solutions (on the right); the lower part shows the corresponding TEM images of the nanoparticles precipitated on the tube bottom.[137] (*b*) Fractionation of a sample of nanorods in a stepwise gradient of glycerol concentrations and TEM images of the first major fraction taken from the tube after the separation (above) and the same before separation (below). (*c*) Example of variation of the extinction spectra of Au nanorods upon the change in the surfactant concentration. (*d*) TEM images of nanoparticles in the supernatant and in the precipitate after incubation in a concentrated surfactant solution. Published with permission from ACS Publications.

nanorods that we consider to be most efficient. This approach implies generating conditions under which nanorods lose their colloidal stability and aggregate, whereas particles of other shapes remain stable (Fig. 16 *c*,*d*). These conditions can be attained by using high concentrations of surfactants [138] or by adding sodium chloride and ethanol.[139] Among other methods, note the process proposed for purification of long nanorods by selective chemical dissolution of by-products.[140]

For the plasmonic photothermal therapy using Au nanorods,[141] an important issue is the optimal size of the particles that produce the maximum absorption cross-section per unit weight.[142] In the case of colloidal ensembles of particles, maximizing the efficiency of absorption (or extinc-

tion) depends on the form of size and shape distribution functions of the particles. Miller *et al.*[143] considered the issue of maximizing the optical efficiency of an ensemble of gold nanorods. Using the optical theorem,[27] the authors derived the upper bounds for extinction, absorption and scattering cross-sections per unit volume of the particles

$$\frac{C_{\text{ext}}}{V} \leqslant (1-\eta)kf \tag{25}$$

$$\frac{C_{\text{sca}}}{V} \leqslant \eta(1-\eta)kf \tag{26}$$

$$\frac{C_{\text{abs}}}{V} \leqslant (1-\eta)^2 kf \tag{27}$$

where $\eta = P_{\text{sca}}/P_{\text{ext}}$ is the lower bound for the ratio of the scattered power to the extinction power (radiative efficiency), $k = n_{\text{m}}\omega/c = 2\pi n_{\text{m}}/\lambda$ is the wavenumber in a medium with refractive index $n_{\text{m}} = \sqrt{\varepsilon_{\text{m}}}$, and f defines the dependence of the plasmonic response on the optical susceptibility of the material (χ)

$$f = \frac{|\chi|^2}{\text{Im}(\chi)} \tag{28}$$

Relations (25)–(27) are applicable to any ensemble of dilute or even interacting scatterers of diverse size and shape. Actually, their domain of validity is the same as that of the microscopic electrodynamic description in terms of bulk material susceptibility. In the case of small particles in which the optical susceptibility depends on the size, shape and surface properties, the above estimates are inapplicable. For an ensemble of nanorods in the long-wavelength resonance, the use of the dipole nanoantenna model leads to equality to the right-hand sides of relations (25)–(27).

In conclusion of this Section, note excellent review by Wang and co-workers,[144] covering all studies related to Au nanorods including the synthesis and assembly, heterostructures based on them, classical and quantum plasmonics, and applications related to probing, SERS, optoelectronics, photocatalysis, nanobiotechnology and therapy.

5. Gold nanoshells and nanocages

Gold nanoshells are concentric quasispherical nanoparticles with a thickness from a few to tens of nanometres consisting of a dielectric core of several tens to hundreds of nanometres in diameter and a gold shell. It was noted above that the PR of these particles can be tuned by changing the ratio of the dielectric core diameter to the metal shell thickness. The synthesis of Au nanoshells with an Au_2S internal core was first reported by Zhou *et al.*[145] However, the colloidal and optical properties of the obtained particles were far from optimal. Subsequently, Halas and co-workers[146] developed an original approach to the synthesis of gold nanoshells with a silica core. This opened up the way for a broad use of such particles in plasmonics, nanomedicine and diagnostics. This research group published more than 200 papers addressing the synthesis, optical properties and bioapplications of Au nanoshells.[147]

The synthesis includes four main steps (Fig. 17). In the first step, silica nanoparticles are prepared by hydrolytic condensation of tetraethoxysilane (TEOS) in ethanol in the presence of ammonia by the Stöber method[148] (Fig. 17 *a*). The average particle size, which depends on the molar ratio

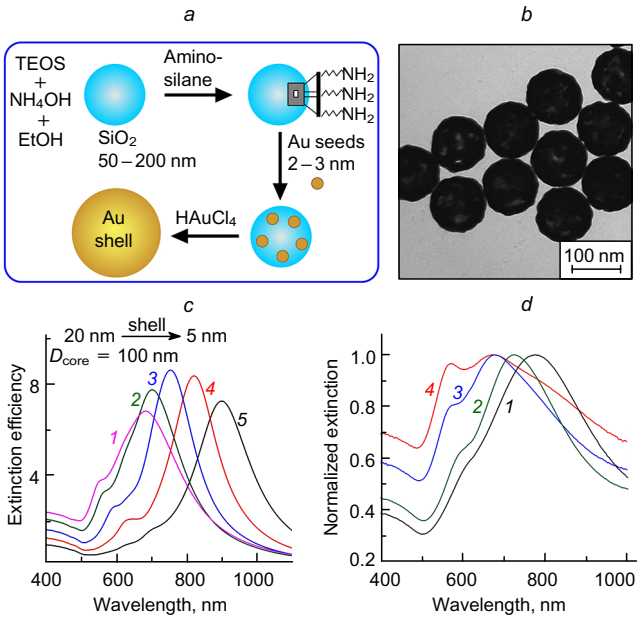


Figure 17. (*a*) Scheme of synthesis of Au nanoshells with a silica core. (*b*) TEM image of GNPs with a core diameter of 116 nm and shell thickness of 16 nm. (*c*) Extinction spectra of Au nanoshells predicted by the Mie scattering theory; the calculation was carried out for shell thickness of 20 (*1*), 15 (*2*), 10 (*3*), 7 (*4*), 5 nm (*5*); for the core size being invariable, a decrease in the shell thickness leads to a shift of the optical resonance to longer wavelengths. (*d*) Experimental extinction spectra of samples with a silica core of 116 nm in diameter and shell thickness of 16 (*1*), 18 (*2*), 25 (*3*) and 34 nm (*4*).[150] Published with permission from Elsevier.

of TEOS and ammonia, can vary from 50 nm to 1 mm.[149] An increase in the ammonia concentration results in the formation of larger particles; a decrease in the TEOS concentration leads to a decrease in the average particle diameter.[150] However, increasing average size induces an increase in the particle polydispersity and polymorphism;[151] meanwhile, the preparation of high-quality nanoshells requires the use of colloids with a standard deviation of the average particle size of $\leqslant 10\%$.[152] Therefore, the range of diameters of the cores obtained by the one-step protocol and suitable for being coated by Au nanoshells is actually 50–250 nm.

The second step includes the surface functionalization of the cores, which is necessary for the subsequent formation of the gold layer. Most often, 3-aminopropyltrimethoxysilane is used to modify the nanoparticle surface.[153] As a result of functionalization, the core surface bears amino groups, which are are positively charged in an aqueous medium; therefore, negatively charged gold seeds are adsorbed on the core surface. Positively charged silica and polystyrene particles can also be obtained by consecutive adsorption of polyelectrolytes on their surface.[154]

The third step of the nanoshell synthesis is adsorption of small particles of colloidal gold on the functionalized core. Usually, small 2–3 nm gold seeds are obtained by the Duff method.[155] Finally, a gold layer is formed in the last step by additional reduction of $HAuCl_4$ on the adsorbed gold nanoparticles. The thickness of the shell depends on the ratio between the core surface area and the amount of reduced gold. The existing protocols result in the formation

of 10 to 50 nm-thick Au nanoshells; with a typical core size of approximately 100–150 nm, this ensures resonance tuning in the range of 600–900 nm (Fig. 17 *b–d*). The preparation of thinner shells is limited by the possibility of filling of the gaps between gold particles during their growth.

In an original publication,[146] sodium borohydride was used as the reducing agent. However, it is known [156] that the nanoshells obtained using strong reducing agents have a rough surface. This significantly reduces the extinction peak to baseline ratio and colloidal stability.[157] A number of reagents have been proposed for the targeted reduction of gold on the adsorbed seeds. Nanoshells with a relatively smooth and fully formed surface can be obtained using hydroxylamine hydrochloride,[158] formaldehyde [152] and many other mild reducing agents. A variety of dielectric materials were used as cores for the synthesis of gold nanoshells: polystyrene particles, benzene nanodroplets, magnetic particles, liposomes and even viruses. However, silica nanoparticles are still used most often as the cores.

Typical TEM images of Au nanoshells on silica cores are shown in Fig. 17 *b*, while Fig. 17 *d* presents experimental extinction spectra of four samples of gold nanoshells with different core diameters and shell thicknesses. According to the Mie theory simulation (Fig. 17 *c*), as the ratio of the core diameter to the shell thickness increases, the maximum in the extinction spectrum is expected to shift to longer wavelengths. The optical spectra of nanoshells on silica cores usually exhibit quite a few doublets and triplets due to partial aggregation in the second step of nanoshell synthesis (functionalization by aminosilanes).[150] This leads to a moderate shift and broadening of the plasmon peak. For the preparation of samples with optical spectra exactly corresponding to the Mie theory, thorough monitoring of particle aggregation or sample separation is required. Guan *et al.*[159] proposed an original one-step procedure for the preparation of gold nanoshells, according to which hydrolysis of 3-aminopropyltriethoxysilane is accompanied by simultaneous growth of silica cores and Au nanoshells. This method is simple for implementation. Although the samples are considerably polydisperse, nanoshells with tunable PR in the 600–850 nm range can be obtained by this method.

A conceptually different strategy using metal particles as templates for porous nanoshells or nanocages was proposed by Sun and Xia.[160] First, polyol synthesis [161, 162] was carried out to obtain silver nanoparticles of various shapes (usually spheres or cubes).[163] Then an aqueous solution of $HAuCl_4$ was added to the resulting nanoparticles, and galvanic replacement of silver atoms by gold atoms was carried out at 100 °C. The standard reduction potential is higher for the $AuCl_4^-$–Au pair (0.99 V *vs.* SHE) than for the Ag^+–Ag pair (0.8 V *vs.* SHE);[160] therefore, gold ions are reduced on the particle surface simultaneously with dissolution of the silver template. When there is deficiency of Au^{3+}, particles with islands of the Au/Ag alloy are formed; as the gold concentration increases, cavities arise in silver particles, thus giving rise to hollow doped nanoshells. In the case of a considerable excess of gold ions, hollow and porous nanostructures appear, which are usually called nanocages.[164] Their appearance is accompanied by a shift in the PR wavelength from 420 nm (typical of silver colloid) to 800–1000 nm, depending on the particle morphology (Fig. 18 *a–f*). It should be emphasized that the term gold nanocages is conventional. Actually, these particles are bimetallic nanostructures of gold and silver, in which the silver content decreases during the synthesis from silver nanocubes from 100% to fairly small values, depending on the degree of galvanic replacement of three silver atoms by one gold atom.

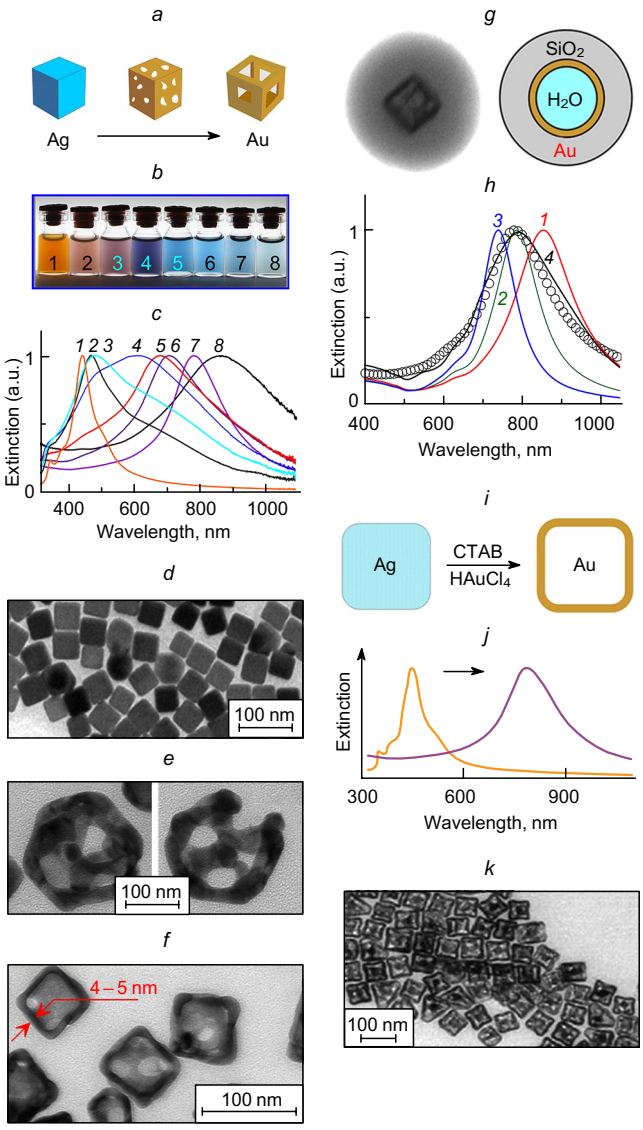


Figure 18. (*a*) Structural changes associated with the galvanic replacement reaction between a silver nanocube and $HAuCl_4$. (*b* and *c*) photo images of samples *1–8* illustrating the conversion of silver nanocubes (left) to gold nanocages (right) and corresponding extinction spectra; nanocage samples were obtained by adding various amounts of an aqueous solution of $HAuCl_4$ to the initial Ag colloid. (*d–g*) Representative TEM images of silver nanocubes (*d*) and gold nanocages (*e*, *f*);[163] geometric shape of silica-coated Au nanocages for Mie theory simulation (*g*). (*h*) Calculated extinction spectra of monodisperse Au nanocages with 60 nm core and gold shell thickness of 3 (*1*), 4 (*2*) and 5 nm (*3*); dots show the experimental spectrum, (*4*) calculation for a polydisperse ensemble of nanocages using a TEM histogram.[165] (*i*, *j*) Scheme of structural changes caused by the galvanic replacement reaction between a silver nanocube and $HAuCl_4$ in CTAB (*i*) and transformation of the extinction spectra during this reaction (*j*). (*k*) Representative TEM images of gold nanocages obtained by this method. Published with permission from Springer (*a–f*) and from Elsevier (*g*, *h*). Figures *i–k* were created by the authors using published data.[166]

Gold nanocages have a more complex structure than simple gold nanoshells on silica cores. In particular, nanocages are often cube-shaped, and their shells, which may consist of a gold and silver alloy, contain pores and cavities. There are also particles consisting only of cube faces. Despite the complexity of the geometric shape, we have shown that the optical properties of such particles can be accurately described using the Mie theory for spherical particles (Fig. 18 *g*,*h*).[165] The crucial factor determining the PR position of nanocages and nanoshells is the ratio of the core diameter to the shell thickness, while the shell structure and shape have a minor effect. Note that using the galvanic replacement reaction, it is possible to obtain very thin (< 5 nm) nanoshells. Hence, the preparation of nanoparticles < 50 nm in size with PR in the near-IR spectral range is possible. A considerable drawback of the method of Sun and Xia[160] is the complexity of the synthesis. First, the preparation of monodisperse silver nanoparticles by polyol synthesis is not an easy task. Second, the galvanic replacement reaction at 100 °C requires thorough control of the rate of addition of reactants.

Maksimova *et al.*[166] proposed a new procedure for the preparation of hollow gold particles; according to this method, the synthesis of silver templates and galvanic replacement reaction are carried out in a solution of CTAB (Fig. 18 *i*–*k*). This approach provides a more facile synthesis of gold nanoshells and nanocages as a result of simultaneous addition of all reactants at room temperature. Apart from using silver templates, protocols including the synthesis of nanocages and nanoshells using cobalt nanoparticles have become popular.[167]

Table 3. Key procedures for the synthesis of Au nanoshells.

Core	Core diameter, nm	Shell thickness, nm	λ_{PR}, nm	Ref.
Au_2S	~25	4–5	600–800	145
SiO_2	70–200	15–50	650–1100	146, 147
SiO_2 or aminosilane	~40	5–10	600–900	159
Ag nanocubes	~50	3–10	600–1000	160–163
Co nanospheres	40	3–5	700–800	167

The main procedures for the synthesis of Au nanoshells with specified geometric and optical parameters are characterized in Table 3.

6. Gold nanostars

Gold nanostars are nanoparticles with a quasi-spherical core and spikes on the surface. The interest in these objects is due to their catalytic and optical properties as well as protocols of synthesis that involve more environmentally friendly and less toxic reactants than those used to obtain other non-spherical particles. Two unique optical features of branched nanostars deserve attention. First, their absorption and scattering properties are less dependent on the orientation of particles and polarization of incident wave than, for example, those of nanorods. A single nanostar is equivalent, in a sense, to a randomly oriented assembly of spikes. Second, owing to the spikes, Au nanostars generate a strong local electric field near the surface, which enhances non-linear and field-dependent properties (for example, Raman scattering).

All synthetic protocols can be classified into two types, those implying seeded (seed-based) and those implying seedless growth; both types have their benefits and drawbacks.‡‡ A qualitative comparison revealed the following differences between these protocols.[24]

Seed-based growth	Seedless growth
Strong dependence on the seed quality	Dependence on the rate of nucleation
Greater control over particle size and morphology	Lower control over particle size and morphology
Slight dependence on the reaction conditions	High sensitivity to reaction conditions
Multistep synthesis	Single-step synthesis
The use of toxic reagents	The use of green reagents

In 2012, Vo-Dinh's research group[168] proposed a new protocol for the synthesis of nanostars without surfactants. The authors used ascorbic acid as a reducing agent and silver ions to induce anisotropic growth conditions. Initially, 15 nm seeds were used in this method, but Khlebtsov *et al.*[169] demonstrated that the size of the final product can be tuned by varying the seed diameter from 3 to 35 nm (Fig. 19).

A thorough study[170] revealed the most critical aspects of the surfactant-free nanostar synthesis. In particular, upon an increase in the number of 5-nanometre seeds in 1 mL of the solution from 2×10^{11} to 3.0×10^{12}, the average core diameter decreases from 93 to 39 nm, the distance between the spikes decreases from 145 to 59 nm, PR wavelength decreases from 800 to 638 nm and the number of spikes decreases from 7–8 to 4–5. Note that in this experiment, other reaction conditions were detected ($AuCl_4^- = 2.5 \times 10^{-6}$ mol and $Ag^+ = 1.02 \times 10^{-7}$ mol). Similar results were also obtained for 12 nm seeds. Finally, a change in the Au^{3+} to Ag^+ ratio in the samples containing 5-nm seeds resulted in the PR wavelength being displaced from 658 to 822 nm and the core size being reduced from 104 to 68 nm.

For understanding the optical properties of Au nanostars, it is useful to compare the absorption and scattering spectra of a 20-spike model and the simplest model of a gold core with only two collinear spikes (Fig. 20). Despite the different morphology, the general spectral characteristics of both models were similar. This means that the critical mechanism underlying the formation of optical spectra is electromagnetic interaction between the spherical core and two collinear anisotropic spikes.

Usually, Au nanostars synthesized by a surfactant-free protocol show one clear-cut plasmon peak between 650 and 1000 nm.[170] Such spectra are most often reported in the literature, while bimodal spectra are encountered as rare exceptions (see, for example, references in a publication by Khlebtsov *et al.*[68]). A possible explanation is that spectrophotometers covering the 1200–2300 nm range are rarely available in laboratories; therefore, the peaks that could occur in the IR region were simply not recorded due to the restricted wavelength ranges of spectrophotometers. Peaks in the IR range were detected (apart from the expected peak

‡‡ These protocols are described in more detail in a review by Siegel and Baker.[24]

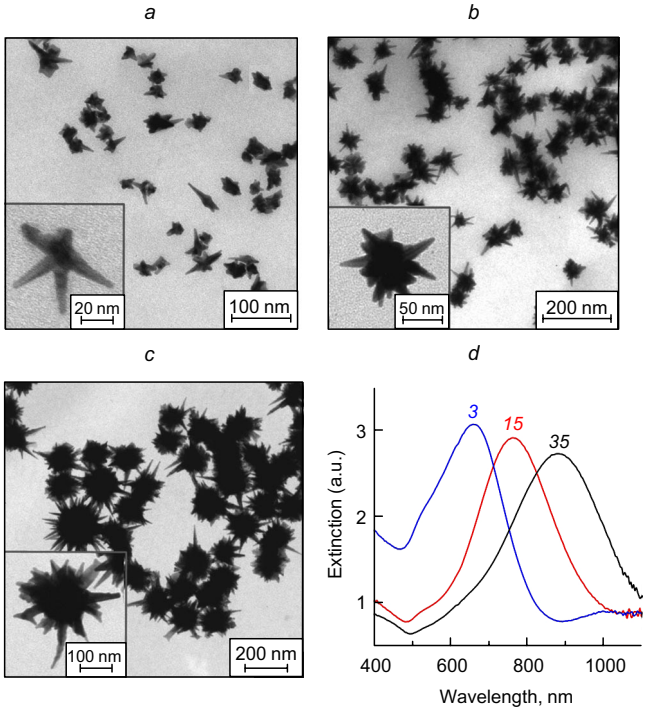


Figure 19. Representative TEM images of samples of Au nanostars prepared using seeds with average diameters of 3 (*a*), 15 (*b*), 35 nm (*c*) and corresponding extinction spectra (*d*). The insets show the enlarged images of typical nanostars.[169] Published with permission from Springer.

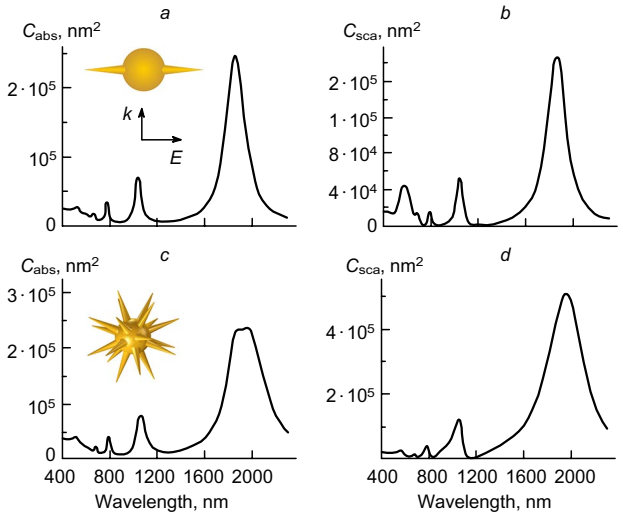


Figure 20. Absorption (*a*, *c*) and scattering (*b*, *d*) cross-sections of 2- (*a*, *b*) and 20-spike (*c*, *d*) Au nanostars. Modelling on the COMSOL platform was carried out with the bulk dielectric function of gold: core diameter of 130 nm; the spike base diameter of 30 nm; total spike length of 130 nm; and spike tip diameter of 4 nm. The Figure was created by the authors using published data.[68]

in the 600–1000 nm range) in the spectra of aqueous solutions of Au nanostar colloids.[68] In order to exclude doubts related to the strong absorption of water in the IR range, possible particle aggregation, *etc.*, additional spectral measurements were carried out using particles adsorbed on a microscope cover glass, *i.e.*, at the glass/air interface.

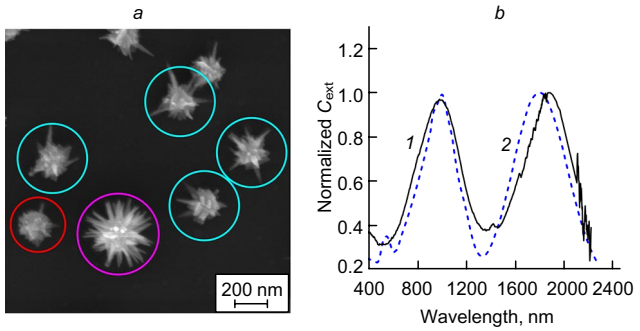


Figure 21. SEM images of Au nanostars of three types (*a*); and experimental (*1*) and simulated (*2*) spectra of the normalized extinction cross-section of nanostars (*b*).[68] In Fig. *a*, particles of the first type are shown in light-blue, particles of the second type are shown in purple, and third type particles are red.

In this experiment, absorption of water was completely ruled out. In this case, similar two-peak spectra were observed, with peaks being shifted, as expected, to shorter wavelengths in comparison with the spectra of aqueous solutions. Thus, bimodal extinction spectra of Au nanostars are associated with their properties.

Considerting SEM images, three types of nanostars were revealed (Fig. 21 *a*).[68] Particles of the first type (~74% of the total amount) are typical Vo-Dinh nanostars with, on average, six asymmetric spikes. Particles of the second type (~12%) are highly symmetrical multispike nanostars with an average number of spikes of ~20. Finally, particles of the third type (~14%) have, most often, small protrusions and 1–2 small spikes. Modelling was carried out using average values for the core diameter, the number of spikes and the spike length and base diameter for each type of particles.[68] It was found that the spike ensemble of the main fraction of stars consists of two sub-ensembles, one composed of long and thin spikes, and the other composed of short and thicker spikes. Since the spikes determine the position of peaks in the extinction spectrum, the presence of two sub-ensembles accounts for the appearance of two peaks in the spectrum. The proposed model provides a satisfactory agreement between the experimental and simulated absorption spectra with correct positions of peaks in the IR and visible regions (Fig. 21 *b*).

Owing to easy synthesis, Au nanostars are used in bioimaging and photothermal and photodynamic therapy. Among other advantages, an important issue is a slight dependence of the absorption and scattering cross-sections on the linear polarization of incident light. However, nanostars are not free from some drawbacks. First, their PR peaks are usually broadened in comparison with, for example, PR peaks of nanorods. Second, samples consist of particles of different morphology and size. Third, the spikes of nanostars tend to be shortened on storage under ambient conditions. Correspondingly, PR shifts to shorter wavelengths on storage. Finally, due to strong local field and heating of the spikes, it is necessary to thoroughly control the radiation power in order to avoid nanostar melting, fragmentation and transformation into spheres.

7. Gold nanorods with a silver shell

The synthesis of anisotropic silver particles with narrow size and aspect ratio distributions is complicated by the insta-

bility of particles in aqueous solutions and poor control over changes in the particle morphology under the action of various factors, including light. According to a more promising strategy, stable gold template particles with desired parameters are first synthesized, and then a silver shell on these particles is formed. Due to the difference between the dielectric functions of gold and silver, the formation of the silver shell is accompanied by a PR shift to shorter wavelengths, which gives a certain degree of freedom in its tuning. This approach was first implemented by Ah *et al.*,[171] who reduced silver from $AgCl_4^{3-}$ ions on the surface of Au nanorods. In later studies,[172, 173] reduction of $AgNO_3$ on Au nanorods was accomplished by ascorbic acid under alkaline conditions. The procedure used by Huang *et al.*[172] afforded dumbbell-like gold–silver nanorods with increased thickness of silver layer at the ends. A more convenient and reliable protocol [173] included the use of polyvinylpyrrolidone as a stabilizer (this method was somewhat modified by Sönnichsen and co-workers [174]). The same stabilization method was used in our study to prepare high-quality gold–silver nanorods;[175] this resulted in a record-high scattered light depolarization in colloids with a random orientation of particles.[176]

In a number of studies (see, for example [177–179]), SERS tags were synthesized using the adsorption of molecules with a large Raman scattering cross-section on an Au nanorod and the subsequent silver coating. It was noted [180] that depending on the concentration of 4-nitrobenzenethiol, cuboid particles or tip-functionalized nanorods (TFNR) are formed (Fig. 22).

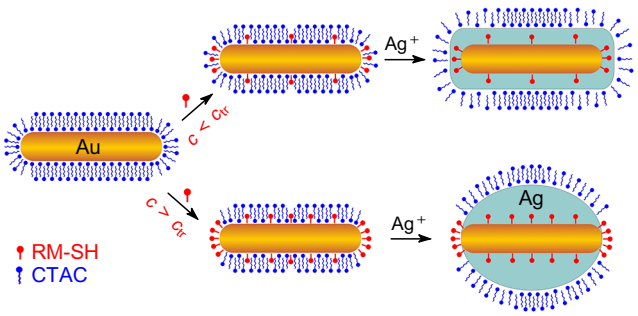


Figure 22. Scheme of formation of Au/NBT/Ag nanostructures (NBT is 4-nitrobenzenethiol) at a concentration of thiolated aromatic Raman molecules (RM-SH) below and above the critical value (c_{tr}).[180] Published with permission from ACS Publications.

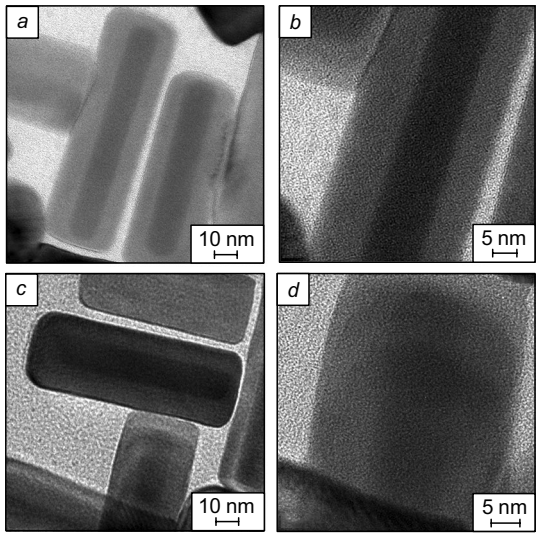


Figure 24. High-resolution TEM images of Au/ATP/Ag nanocuboids with silver layer thickness of 9 (*a*, *b*) and 13.5 nm (*c*, *d*).[178] Published with permission from Springer.

Nanocuboids were obtained using gold nanorods synthesized in a binary surfactant and functionalized with thionitrophenol or 4-aminothiophenol (ATP) molecules. Details of the synthetic procedures can be found in original publications.[178, 180] Conventional TEM images and high-resolution TEM images of Au/ATP/Ag nanocuboids obtained by the synthesis of silver shell on gold nanorods with adsorbed ATP molecules are shown in Figs 23, 24.

The extinction spectrum of Au/ATP/Ag nanocuboids, unlike the spectra of Au rods, has an intricate structure with one longitudinal and three transverse modes (Fig. 25).[181] It was shown [182] that the most intense multipole resonances are excited at four specific incident light polarizations relative to the Au/Ag cuboid frame: longitudinal face diagonal, transverse edge, transverse face diagonal and

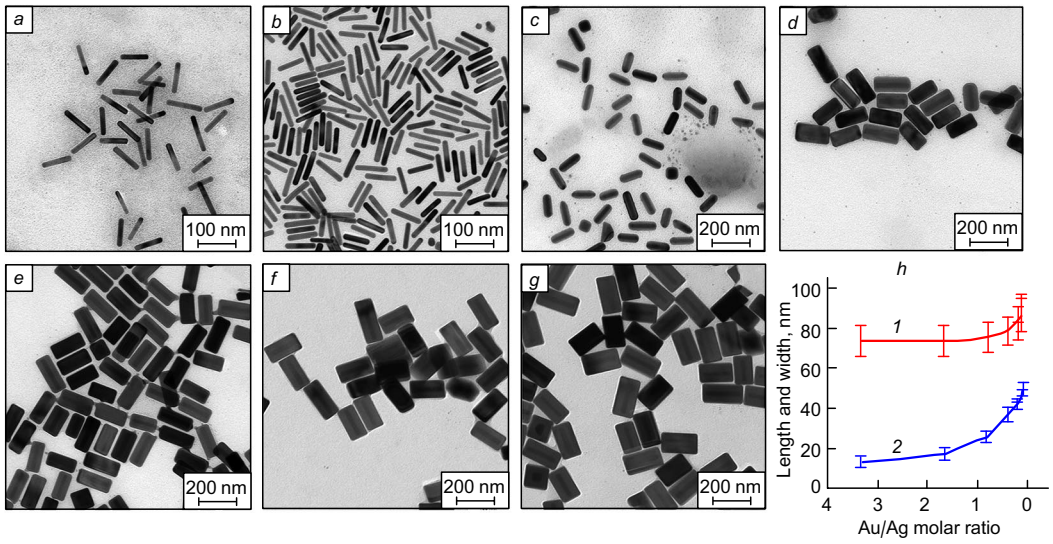


Figure 23. TEM images of Au/ATP/Ag nanocuboids with silver shell thickness of 0.2 (*a*), 0.5 (*b*), 2 (*c*), 5 (*d*), 9 (*e*), 13.5 (*f*) and 16 nm (*g*) and particle length (*1*) and width (*2*) *vs.* Au : Ag molar ratio (*h*).[178] Published with permission from Springer.

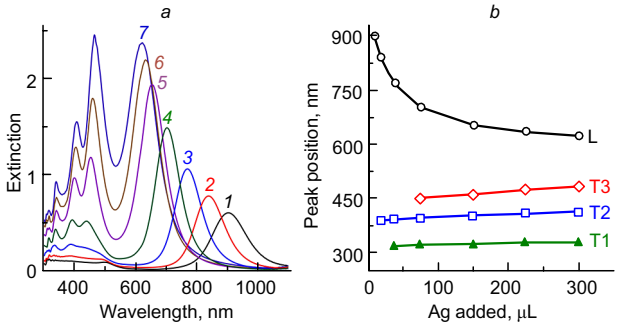


Figure 25. Extinction spectra of Au/ATP/Ag nanocuboids (*a*) and peak positions of longitudinal (L) and three transverse (T1, T2, T3) modes vs. amount of the added silver (*b*).[181] The spectra in Fig. a refer to samples with Ag : Au molar ratio of 0.15 (*1*), 0.25 (*2*), 0.33 (*3*), 0.5 (*4*), 1 (*5*), 1.5 (*6*), 2 (*7*). Published with permission from Elsevier.

cuboid body diagonal polarizations.[§§] In Fig. 25, letter L designates the lowest-frequency dipole mode excited by the light polarized along the longer axis of the cuboid. Besides, three types of transverse modes (T1 – T3) are excited when the light is polarized across the cuboid longer axis. As the amount of silver added to the growth solution increases,[178] longitudinal resonance shifts to shorter wavelengths, while the peaks of multipole modes T1 – T3 shift to longer wavelengths. Thus, this example illustrates the possibility of tuning of not only the lowest dipole mode, but also multipole modes.

If the conditions of synthesis correspond to the formation of particles with an asymmetric silver shell and open gold tips, the multipole modes are no longer detected, and the absorption spectra approximately correspond to usual spectra of gold – silver nanorods and shift to shorter wavelengths as the shell grows (Fig. 26).[180] When the silver layer is thick, the contribution of the asymmetrical gold core becomes less pronounced, and the most intense dipole peak is formed at approximately 450 nm. The spectra shown in Fig. 26 demonstrate a unique case of the most broad plasmonic tuning in the wavelength range from 950 to 450 nm (nearly an octave), which would be impossible by changing only the particle shape.

The strong SERS signal upon laser excitation outside PR distinguishes TFNR tags from their analogues. In order to show this explicitly, we measured SERS spectra for various NBT-functionalized nanoparticles with PR wavelength either shorter than (or equal to) or slightly greater than 785 nm, that is, the laser excitation wavelength (Fig. 27 *a*,*b*). For comparison, we chose gold nanorods with PR at 700 and 810 nm (the aspect ratio of ~3 and ~3.8, respectively) and nanostars with PR at 650 and 785 nm (Fig. 27 *b*). As reference samples, silver-coated Au nanorods designated in the original study [180] as TFNR/Ag4 and TFNR/Ag16 were used (Ag4 and Ag16 correspond to 4 and 16 nm thick silver layers). Their extinction spectra (Fig. 27 *b*, curves *5* and *6*) showed a resonance at 785 nm (TFNR/Ag4) and two long-wavelength resonance peaks at 550 nm (TFNR/Ag16). The contents of particles in the samples were normalized to the total gold concentration (1 mmol L^{-1}). Thus, a set of SERS tags with resonance and off-resonance excitation was analyzed.

The measured SERS spectra are depicted in Fig. 27 *c*. For gold nanorods and nanostars, the highest intensities were detected upon the resonance excitation. However, for TFNR tags, the maximum signal was obtained for the off-resonance excitation of the TFNR/Ag16 sample. Moreover, the SERS signal intensities were the highest for this sample among other samples studied. An important feature of the measured TFNR/Ag16 spectrum is the absence of the

[§§] Polarizations along the longitudinal and transverse faces described by Yang *et al.*[182] correspond to TM and TE polarizations [181] where light is polarized along and across the cuboid axis.

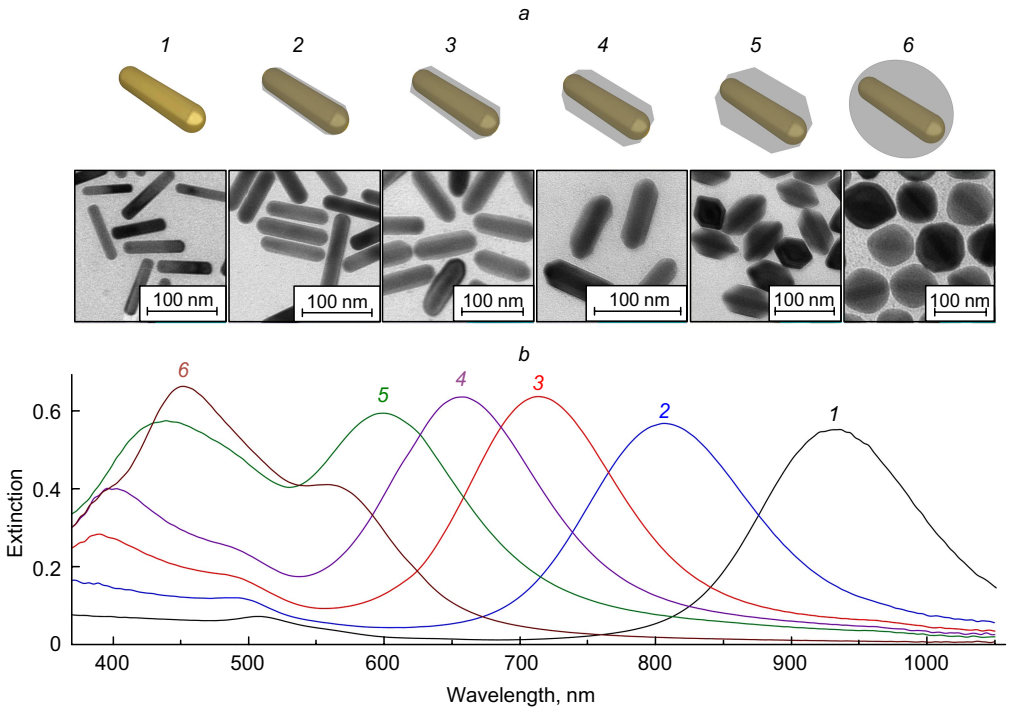


Figure 26. Variation of the shape and TEM images of TFNR samples (*1*–*6*, see text) with increasing thickness of the silver shell (*a*) and corresponding extinction spectra (*b*).[180] Published with permission from ACS Publications.

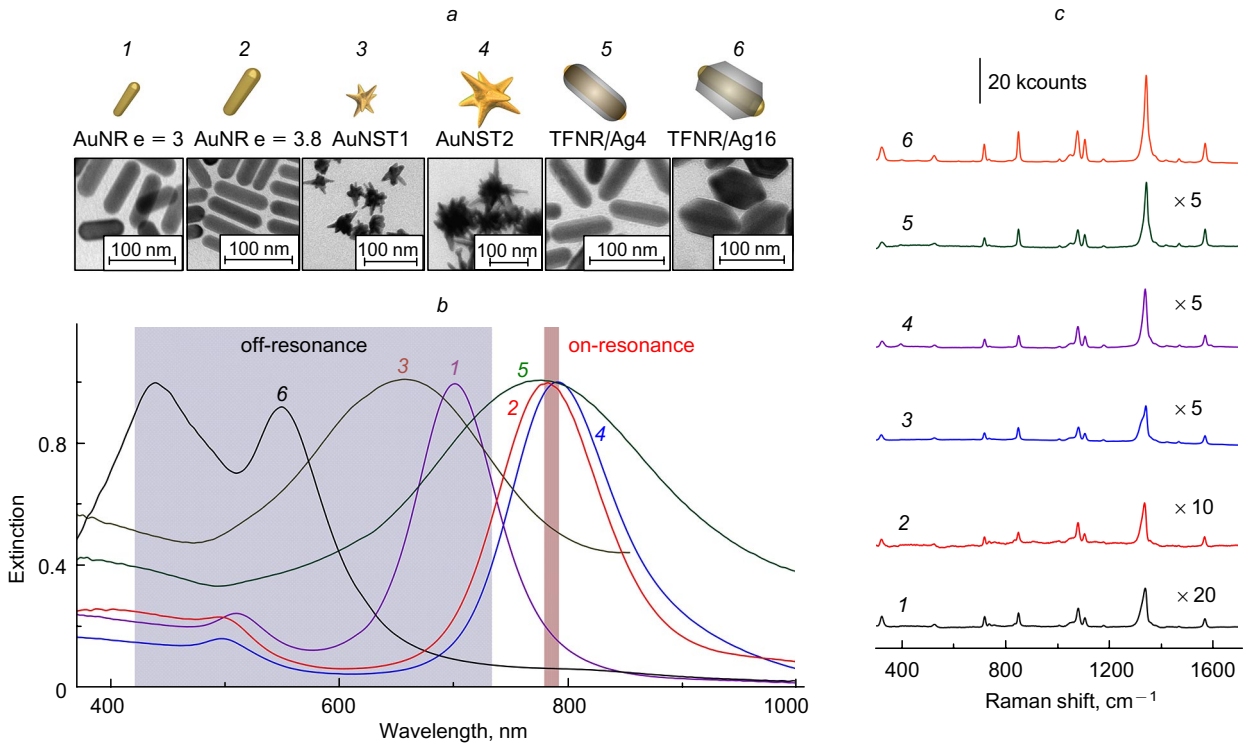


Figure 27. Schematic and TEM images of samples of NBT functionalized nanorods, gold nanostars, TFNR/Ag4 and TFNR/Ag16 particles (*1*–*6*) (*a*), and their extinction (*b*) and SERS spectra (*c*); here e is the rod aspect ratio.[180] Published with permission from ACS Publications.

background fluorescence signal, which was recorded for the tags based on Au nanorods.

The data depicted in Fig. 27 bring about an important question of existence of an optimal structure of Au/NBT/Ag probes for TFNR with a silver layer thickness providing for the most intense SERS signal. This question can be answered by analyzing the evolution of the extinction spectra and the peak intensity at 1345 cm^{-1} with increasing concentration of $AgNO_3$ in the reaction mixture during the synthesis of the probes (Fig. 28). An increase in the $AgNO_3$ concentration results in a regular increase in the silver shell thickness, which in turn induces a short-wavelength shift of the principal PR peak and gives rise to bimodal spectra. The initial Au nanorods (sample *1*) have PR at 930 nm, which is markedly greater than785 nm (laser wavelength in the SERS measurements); next (sample *2*) PR almost coincides with 785 nm; and then it shifts to the shorter-wavelength off-resonance excitation region. As the shell thickness increases, the spectrum becomes bimodal, with the second strong peak being at 450 nm. The key result is shown in Fig. 28 *b* as the concentration dependence of the normalized intensity of the SERS peak at 1345 cm^{-1}, I_{TFNR}/I_{NR} (normalization to the intensity of the line of the initial particles). As can be seen, the optimal structure of the Au/NBT/Ag particles, in which the SERS line is ~55 times more intense than the line of the initial Au nanorods, actually exists. This structure is formed when the concentration of the added $AgNO_3$ is 0.5 mmol L^{-1} (sample *5*) and the silver shell thickness reaches ~15 nm.[180]

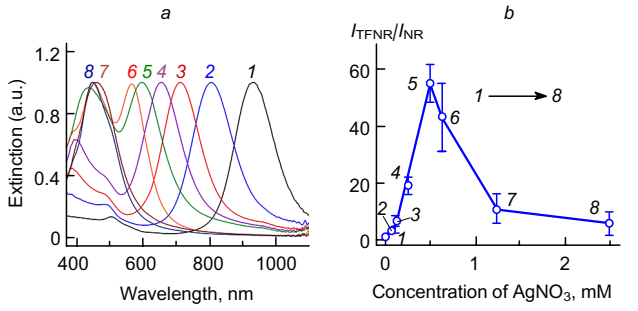


Figure 28. Extinction spectra of Au/NBT/Ag particles (*a*) and normalized SERS peak at 1345 cm^{-1} *vs.* the amount of $AgNO_3$ added to the reaction mixture during the silver shell synthesis (*b*). Concentration of $AgNO_3$, mmol L^{-1}: (*1*) 0 (initial sample), (*2*) 0.0625, (*3*) 0.125, (*4*) 0.25, (*5*) 0.5, (*6*) 0.625, (*7*) 1.25, (*8*) 2.5. Dots *1*–*8* in Fig. *b* correspond to spectra *1*–*8* in Fig. *a*.[180] Published with permission from ACS Publications.

8. Applications of nanoparticles of various size, shape and structure

Unique optical properties of gold and silver nanoparticles and their composites are now widely utilized in various technological applications such as plasmonic photothermal therapy, biosensorics, near-field optical microscopy, single-electron transistors, SERS, catalysis, plasmon-induced reactions, and so on.

A highly important application of plasmonic nanoparticles is photothermal therapy, which uses effective conversion of light energy to heat, which can induce apoptosis and necrosis of cancer cells. An important advantage of plasmonic PTT is that nanoscale heat evolution occurs locally, unlike, for example, heat evolution induced by conventional radiofrequency radiation heating. Among the developed PTT nanoplatforms, functionalized Au nanorods are used most frequently.[183–193] The biocompatibility and biotargeting of nanorods were attained *via* functionalization by antibodies and aptamers and also by various biopolymers,

including albumin,[194] cell membrane components,[195] peptides,[196] polyTLR7/8a,[197] DARPin_9–29 (Ref. 198) and so on. Besides coating by mesoporous silica,[199,200] another method that seems promising is encapsulation of Au nanorods into biodegradable polymer matrices and liposomes. This approach was used, for example, for the fabrication of a nanocomposite ensuring a targeted controlled release of ruthenium(II) polypyridyl complexes.[201] The huge body of data on various applications of Au nanorods, including PTT, can be found in a number of reviews.[144, 202–204]

Pioneering studies on the use of functionalized Au nanocages in biomedicine were reported by Xia's research group.[205] A number of papers published to date describe the use of conjugates of Au nanocages in in vitro laser-induced PTT of malignant neoplasms [206,207] and in the laser-induced plasmonic PTT of grafted tumours in animal models.[208–212] Data on applications of the bioconjugates of Au nanocages are summarized in a review.[213]

The plasmon resonance of Au nanostars occurs in the near-IR spectral range; therefore, they can be used in the plasmonic PTT as effective convertors of light to heat.[24,214] For example, Crawford *et al.*[215] described the use of PTT with Au nanostar conjugates for ablation of the inflammatory breast cancer tumor. Espinosa *et al.*[216] injected stars directly into PC3 tumour induced in mice for the subsequent PTT; members of the Vo-Dingh's research group [217,218] were the first to use PTT with Au nanostars in combination with immunotherapy.

Considering the geometric parameters and plasmonic properties, Au nanoshells with SiO_2/Au structure do not appear highly efficient PTT agents. Nevertheless, among numerous representatives of plasmonic nanostructures, only these particles have passed three phases of clinical trials (Nanospectra Biosciences company, USA). The registered AuroLase® drug was tested as a PTT agent for the treatment of refractory/recurrent head and neck tumours and metastatic lung cancer.[219] However, the results of testing were ambiguous. The review by Vilches and Quidant [219] reported also the beginning of the third phase of clinical trials of plasmonic PTT of the localized prostate cancer.[220] In this case, the Au nanostars were used in PTT under control of magnetic resonance and ultrasonic imaging. Preliminary results were good; however, to draw final conclusions about the long-term efficacy of PTT and possible adverse events, further research is required.

The investigations and applications of plasmonic PTT over the last 15 years (starting from the pioneering studies carried out in 2004–2008 by research groups of Halas, El-Sayed, von Maltzan and other) demonstrated that translation of model experiments to clinical practice cannot be generally called successful.[221,222] Therefore, certain hopes are placed on combined approaches in which simultaneous use of different types of cancer therapy could produce synergistic effect.[223,224] Bucharskaya *et al.*[11] named five types of combined therapeutic approaches, which combine PTT with PDT, chemotherapy, immunotherapy, gene therapy and radiotherapy.

The first approach was developed by Yuan *et al.*,[225] who devised multifunctional nanocomposites based on porous Co_3O_4 nanoparticles. Owing to the multifunctional modality, composites were used as contrast agents in the photoacoustic and magnetic resonance imaging and also as PTT and PDT agents activated by near IR radiation. Moreover, suppression of the epithelial–mesenchymal transition pathway by Co_3O_4 nanodiscs was demonstrated.

A combination of PTT and PDT techniques can potentially be based on not only the use of PDT agents and plasmonic nanoparticles, but also generation of singlet oxygen by many nanoparticles,[226–228] bipyramids,[229] nanocages [230] and nanoshells.[231] However, the efficiency of this generation is an open question.[¶¶]

Combining chemotherapy with PTT leads to some beneficial synergistic effects, including more efficient penetration of cytostatics into cancer cells, some mitigation of the side effects of chemotherapy, more effective suppression of the tumour growth, and decrease in the multidrug resistance.[233] A synergistic increase in the cytotoxicity was also found for chemotherapeutic drugs such as carmustine, carboplatin, cyclophosphamide and cisplatin. In particular, as the temperature of the tumour is raised from 37 to 40–43 °C, the cytotoxicity increased, with the gain being approximately proportional to the temperature increment.[10,234] One of the reasons for decreasing the PTT efficiency is activation of heat shock proteins, which increase the resistance of cancer cells to elevated temperatures. The decrease in the efficiency of PTT via activation of thermal shock proteins is especially pronounced in the case of heterogeneous tumours and poor penetration of laser radiation into deep layers caused by scattering and absorption of the radiation. In these situations, the combination of PTT and chemotherapy by encapsulation of the dosage form and PTT agent into the same nanoconstruct may produce a significant synergistic effect and suppress the main drawback of chemotherapy — severe side effects.

The advantage of immunotherapy over other strategies that imply external physical and chemical impacts is the use of internal resources of the patient's immune system. Usually, cancer cells decrease the stimulation of T-lymphocytes and thus switch off the immune protection.[235] When dendritic and T-cells enter the lesions, the activation of the antigen-specific immune response is hampered by the immunosuppressive action of the microenvironment of the tumour. The principle of immunotherapy is the activation of immune cells capable of infiltration into the tumour by activating the antigen-specific immune response to the specific antigens released by cancer cells. PDT can stimulate the immunogenic cell death, which is due to the appearance of molecular patterns related to cell damage. Turubanova *et al.*[236] reported the PDT-stimulated enhancement of immunogenic cell death; therefore, combination of PDT and immunotherapy may prove to be useful. Data on successful combination of immunotherapy and PTT are still scarce,[218,237,238] and it is not entirely clear how PTT can stimulate the efficiency of immune response.

Further, it was shown that local photothermal treatment of a tumour with near-IR light in the second transparency window is a promising strategy for triggering in situ tumour vaccination for the treatment of cancer. However, low penetration of photothermal agents into tumours markedly decreases their spatial effect on the formation of sufficient amounts of tumour-associated antigens, which is a key factor for the success of vaccination. In a study by Chen *et al.*,[239] a nanoadjuvant system was fabricated on the basis of Au nanostars decorated with hyaluronidases and immu-

[¶¶] In particular, our research group detected the generation of singlet oxygen by fluorescent Au nanoclusters comprising ~25 gold atoms. However, the efficiency of such generation cannot even come close to the efficiency of generation of singlet oxygen by well-known PDT agents such as chlorin E6.[232]

nostimulating CpG oligodeoxynucleotides. Nanoadjuvant is able to deeply penetrate into the tumour by loosening the dense extracellular matrix. On irradiation with near-IR light, the nanoadjuvant considerably inhibits the tumour growth, induces a cascade of immune responses, forms a pronounced adaptive immunity against re-infection, enhances the abscopal effect and completely inhibits lung metastases. The adjuvant properties of GNPs [240, 241] can be used for both immune and combined therapy of cancer. It was shown that the efficacy of GNPs as adjuvants decreases in the series

50 nm GNPs > 15 nm GNPs > Au nanoshells >
> Au nanostars > Au nanorods

The gene therapy is based on stimulation of cancer cell apoptosis, increase in the cytotoxic immune cytokine level and suppression of the expression of heat shock proteins. Yet another aspect is associated with possible PTT-induced improvement of DNA and RNA delivery to the cells [242] (usually these molecules are damaged by enzymes). In addition, the possibility of enhancing the suppression of gene expression due to increased endosomal escape of gene delivery vectors is being considered.[243] Currently, there is no enough data for translation of combined PTT and gene therapy to clinical practice due to biocompatibility problems and toxicity of nanostructure components.

Radiotherapy, meaning treatment using ionizing radiation (X-rays, γ- and β-radiation, neutron radiation, beams of elementary particles), differs from optically induced PTT and PDT by deep penetration of the radiation into tissues due to a much lower extinction of waves. Therefore, radiotherapy guided by computed tomography has become a proven clinical method.[244] The main obstacle hampering the extensive use of radiotherapy with low level of exposure to photon/electron beams is tumour hypoxia, which reduces the DNA damage induced by reactive oxygen species. The results of studies [245, 246] give hope for successful solution of this problem owing to synergistic therapeutic effect of combined PTT and radiotherapy.

A lot of experimental and theoretical data have been accumulated on SERS of molecules located near a metal surface.[247, 248] A highly promising application of SERS is the study of structural and functional features of biological molecules of various classes, such as amino acids; nucleic acids and bases; water-soluble, membrane and light-sensitive proteins; immune complexes; whole cells (bacterial, tumor and other cells); pharmaceuticals, *etc*.[249] The authors of most studies used adsorption of biological molecules on metal electrodes or thin films. However, methods in which colloidal metals (most often, gold and silver) and their aggregates or assemblies are used for signal amplification become more and more popular.[250] The amplification is determined by giant nonlinear local fields arising in metal clusters.[248]

The SERS signal efficiency is crucially affected by the nanoparticle shape and size (larger nanoparticles produce more intense signals).[251] Methods based on SERS use morphologically diverse nanoparticles: spheres, rods, cubes, triangles, stars and shells (both Au/SiO_2 and SiO_2/Au). It was proved that anisotropic nanoparticles have a clear advantage for highly sensitive (down to zeptomolar) detection of analytes, especially in complex solutions such as biological or environmental samples.[252, 253] For example, Tian *et al*.[254] showed that SERS effect is enhanced in the following series:

nanostars > nanotriangles > nanosphere aggregates >
> nanospheres

Gold nanoparticles with spiky faces such as concave nanocubes, nanotrioctahedra and nanostars are optimal for single-particle SERS upon near-IR excitation.[255]

Silver-coated GNPs of various morphology were also proposed for amplification of SERS signal; in this case, SERS efficiency is higher than that attained with uniform gold nanoparticles, and it can be tuned by varying the silver shell thickness.[256–259] In order to attain sufficiently high signal intensity, tunability and biocompatibility, all components of SERS nanostructures must be rationally designed and adapted to a specific application. The design parameters should include fine tuning of plasmonic core properties, optimization of the Raman reporter molecule, properties of the surface coating, size of the gap between the core and shell (or shells in the case of multishell nanoparticles).[260–262]

Owing to considerable progress in the design of simple and robust techniques for the synthesis of GNPs of various size and shape (see above) and for functionalization of their surface, the SERS applications of GNPs have been markedly extended, covering, in particular, biosensorics, immunoanalysis, bioanalytics, bioimaging and medical diagnosis in vitro and in vivo (see original studies [263–266] and comprehensive reviews [267–269] devoted to biomedical applications of SERS).

Gold is an inert element, which was long considered inapplicable for catalysis. However at the turn of the 21st century, gold was successfully used as a catalyst in ethylene hydrochlorination, low-temperature CO oxidation, nucleophilic addition to a triple bond, C—C bond formation reactions, synthesis of compounds with double bonds, *etc*.[270–273] Later, data on the catalytic activity of mono- and bimetallic gold-based nanoparticles were reported. The developed reactions include CO oxidation, aerobic oxidation of mono- and polyhydric alcohols and alkanes, selective hydrogenation of alkynes, hydrogenation of nitroaromatic compounds, hydrogenation of CO_2, C—C bond formation, methane oxidation, electrolytic production of hydrogen, dehydrogenation of dimethylaminoborane at room temperature, glycerol oxidation and other reactions, mainly hydrogenation and oxidation reactions.[274–276] Gold nanoparticles of various sizes and shapes are used as catalysts; nanospheres of 3–5 nm in diameter supported on mesoporous SiO_2 or CeO_2 are most popular.[276, 277]

Plasmon-induced reactions using GNPs are close to catalyzed reactions. The excitation of localized surface plasmons in noble metal nanoparticles brings about nanoscale effects such as electric field enhancement, generation of hot electrons and temperature rise near the surface. Light absorption by a metal surface plays a key role in the induction of photochemical reactions of adsorbed molecules. The ability to control absorption cross-section and energy of absorbed light for metallic plasmonic nanoparticles offers new opportunities for the control of photochemical reactions. Irradiation of GNPs at their plasmon resonance frequency gives rise to a high plasmon charge and leads to a considerable temperature rise, which may be used to initiate catalytic reactions. These effects are used, in particular, for the polymer synthesis by photopolymeriza-

tion of pyrrole monomers, dehalogenation of brominated purine nucleobases, transformation of 4-nitrobenzenethiol, keto–enol isomerization, production of hydrogen gas, synthesis of 4,4′-dimercaptoazobenzene, *etc.*[278–280]

9. Conclusion

Despite the long history of research, gold-based nanoparticles are still a relevant object of fundamental and applied studies. Full implementation of biomedical and technological potential of plasmonic Au nanoparticles requires reliable methods for their synthesis with precisely controlled size, structure and morphology. By varying the geometrical size, structure and composition of particles, one can attain full control over the optical properties, including the PR wavelength and absorption and scattering cross-sections. This review discusses the most reliable modern protocols and their updates, which are currently used in many laboratories around the world.

Hundreds (if not thousands) of publications describe various protocols for the synthesis of gold and hybrid (including bimetallic) particles. However, only three types of Au nanoparticles, spheres, rods and stars, are in most demand for real applications. Gold nanospheres remain subjects of fundamental and applied studies, and existing methods of their synthesis considerably surpass in efficiency the Borovskaya – Turkevich – Frens classical citrate method. Synthetic routes to high-quality ideally spherical and almost monodisperse particles with diameters ranging from 5 – 10 to 250 nm have now been developed. There are green processes for GNP synthesis with simultaneous functionalization by biocompatible ligands. A drawback of Au nanospheres for biological applications is PR position in the spectral region corresponding to absorption of blood and biological tissues. Nevertheless, this does not affect biosensoric applications.

Regarding precise PR tuning over a broad range from 1200 to 600 nm, *i.e.*, within an octave, Au nanorods have no competitors among plasmonic particles. Owing to efforts of researchers, specialists have at their disposal reliable protocols for the reproducible synthesis, overgrowth and chemical etching of Au nanorods, with their diameters being controlled in the 10 to 50 nm range and their length being controlled from 30 to 120 nm. For example, using the Vigderman – Zubarev method, it is convenient to synthesize a large amount of nanorods with PR at 1100 nm wavelength and then perform chemical etching to obtain samples with equal particle concentration, identical cigar-like morphology and PR wavelength tuning with an accuracy of several nanometres. There are no other particles with analogous parameters that can be so easily prepared. Due to these advantages, the use of Au nanorods is described in many applied papers. Several companies, *e.g.*, Nanopartz (https://www.nanopartz.com), set up the production of gold nanospheres and nanorods on a commercial scale; hence, they can be simply purchased and not synthesized. While listing the benefits of Au nanorods, one cannot but mention their two drawbacks. Plasmonic properties (absorption and scattering cross-sections, local fields) depend strongly on the particle orientation relative to the linearly polarized incident light. Therefore, the average extinction cross-section of the colloid at the PR wavelength is $\sim 1/3$ of the maximum extinction cross-section in the longitudinal resonance. If the light is not polarized, this difference is eliminated. The most severe drawback of Au nanorods regarding biological applications is the presence of toxic stabilizing CTAB molecules that are adsorbed on the particle surface during the synthesis. CTAB cannot be removed by mere washing, as particles would aggregate; therefore, it is necessary to replace CTAB molecules by biocompatible molecules of thiolated polyethylene glycol, the thiol groups of which chemically bind to gold and displace CTAB from the surface.

The studies addressing the synthesis and applications of Au nanoshells are less numerous than the literature devoted to Au nanorods. The size and the ratio of absorption and scattering cross-sections of Au nanoshells are not highly suitable for biological applications. Their absorption and extinction spectra are very similar to analogous spectra of Au nanostars, for which there are convenient and facile synthetic protocols with size control. A drawback of nanostars is a certain temporal instability of the spike morphology, resulting in time drift of optical properties. Nevertheless, they are used rather widely due to the ease of their synthesis.[24, 206, 214–216, 238, 281, 282]

The protocols of synthesis of Au nanocages by galvanic replacement of silver atoms in silver nanocubes have not gained popularity due to the complexity of high-temperature synthesis. Furthermore, the extinction spectra of nanocages and nanostars are very similar. The only potential advantage of gold – silver nanocages is the possibility of tuning PR wavelength from blue ($\sim$430 nm) to red ($\sim$800 nm) electromagnetic spectral range, *i.e.*, within almost an octave. However, since biotissues and cells of organisms absorb in the blue and green regions, these advantages are not utilized. As it has been noted above, instead of high-temperature synthesis, a simple single-step method [166] implemented at room temperature can be used to obtain nanocages. The extinction spectra thus obtained differ little from the spectra of classical nanocages. Despite the noted drawbacks, studies on PTT applications of Au nanocages are still in progress.[205–213, 283]

In the presence of alternative choices for a PTT nanoplatform, there arises an important issue of comparing the efficiency of different particles towards the conversion of light to heat. Khlebtsov *et al.*[163] reported a comparison of the PT efficiency of three types of nanoparticles: Si_2O/Au, Au nanocages and Au nanorods. The plasmon resonance of all particles was tuned to the wavelength of the semiconductor laser (810 nm). When colloids were irradiated in a centimetre cell from top to bottom, the most pronounced heating was observed, as expected, at a certain distance from the entrance of the beam into the colloid. The particle efficiency was evaluated from the kinetics of heating of the suspension and the maximum stationary temperature. The absorbances of colloids at 810 nm were approximately equal, and the curves of heating kinetics differed little from one another, but Au nanorods still showed the best efficiency. However, determination of PT efficiency per metal weight of one nanoparticle resulted in the following sequence:

Au nanocages > Au nanorods > SiO_2/Au

The conclusion drawn by Khlebtsov *et al.*[163] about the better PT efficiency of Au nanorods and Au nanocages compared to that of SiO_2/Au is in line with the results of von Maltzahn *et al.*[284] and Rengan *et al.*,[285] respectively.

Pattani and Tunnell [286] carried out a comparative study of the PT efficiency of gold nanorods and nanoshells using an advanced procedure for data measurement and analysis

and also the approach developed by Roper *et al.*[287] In the study by Pattani and Tunnell,[286] the absorption cross-section was higher for Au nanoshells than for Au nanorods. Correspondingly, for the same nanoparticle concentrations, Au nanoshells heated the colloid more efficiently. However, when calculated per unit metal weight, the general efficiency of the conversion of light to heat was approximately two times higher for Au nanorods than for Au nanoshells.

The effect of nanoparticle shape on the efficiency of PTT of cancer was studied by Yang *et al.*,[288] who synthesized three types of gold particles, nanorods, nanostars and nanoshells, and functionalized them with thiolated polyethylene glycol. The goal of the study was to compare and evaluate the PTT of tumours upon laser irradiation at 810 nm. The best results were found for nanostars. These results agree with the data of Pylaev *et al.*,[289] who showed high efficiency of laser plasmon-induced optoporation of cells grown on a monolayer of Au nanostars in a culture plate.

Yang *et al.*[290] compared the PT efficiency of gold nanospheres, nanoflowers, nanorods and nanocages. Nanoflowers showed the highest PT efficiency, which decreased in the following sequence of gold nanoparticles:

flowers > spheres > cages > rods

Note that the performance characteristics refer to different PR wavelengths; hence, Au nanospheres cannot actually be used for the near-IR range. As shown above, the minimum efficiency of Au nanorods found in this study is at variance with other data. The conclusion about the highest specific PT efficiency of Au nanocages is consistent with the results of Robinson *et al.*,[208] who evaluated the efficiency of the PTT of prostate cancer using gold nanoparticles shaped as nanocages and nanorods. With the total weight of Au nanocages being 18 times lower than the weight of Au nanorods, the two types of particles showed equal PTT efficiencies. In addition, it was noted that the biodistribution and excretion were more optimal for nanocages than for nanorods. A comparison with the data of von Maltzahn *et al.*[284] showed a discrepancy in the conclusions and the necessity of additional, more thorough comparisons. For example, the conclusion made by Yang *et al.*[290] about the maximum efficiency of Au nanocages is not supported by the data of Wang *et al.*,[291] who studied the PT efficiency of gold nanorods, nanocages and also particles that were called nanohexapods. In the authors opinion, the last-mentioned particles proved to be the most efficient PT agents; they showed the best biodistribution and uptake by body cells. However, their study addressed breast cancer rather than prostate cancer, which was treated in the experiment discussed above. It can be seen that in this case, too, the results of different authors are not in line with one another. As one more example, consider the data of Feng *et al.*,[186] who compared the efficiencies of PTT and PDT of gold nanocages, nanoshells and nanorods with equal PR at 808 nm. Having compared the data obtained for living cells and animal models, the authors concluded that the highest PDT efficiency was inherent in nanocages and the lowest efficiency was characteristic of nanorods.

Thus, it follows from the above that this important issue should be further investigated. Apparently, the discrepancy between the results of different research groups is due to the lack of evaluation standards, the development of which seems to be a priority. A similar situation was observed previously for toxicity and biodistribution measurements:[292] the results were contradictory until investigation standards were introduced.

We hope that the subject matter we addressed and citing of the most robust protocols for the synthesis of gold nanoparticles would be of interest and utility to specialists working at the boundary between nanotechnology and biomedicine. Gold nanoparticles are in demand as potential phototherapeutic agents, in particular, as parts of more complex composite nanostructures — molecule-recognizing carriers and anticancer agents. Currently, this field of nanooncology is being actively developed, since the initial hope for the passive targeting of nanoparticles to tumours[293] did not come true.[294] The subsequent development of the nanooncology may include combination of different techniques that are discussed in the present review.

This review was prepared with the financial support of the Russian Science Foundation (Project No 18-14-00016П, parts 1, 2, 4–9; Project No. 19-14-00077, parts 3, 8).

10. List of abbreviations and symbols

ATP — 4-aminothiophenol,
CTAB — cetyltrimethylammonium bromide,
CTAC — cetyltrimethylammonium chloride,
GNPs — gold nanoparticles,
IR — infrared,
NBT — 4-nitrobenzenthiol,
pDDA — poly(diallyldimethylammonium chloride),
PDT — photodynamic therapy,
PR — plasmon resonance,
PT — photothermal,
PTT — photothermal therapy,
SEM — scanning electron microscopy,
SERS — surface-enhanced Raman scattering,
TEM — transmission electron microscopy,
TEOS — tetraethoxysilane,
TFNR — tip-functionalized nanorods,
UV/Vis — ultraviolet/visible spectral range,
a — radius of spherical particle,
a_1 and a_2 — radii of the core and the shell of a two-layer particle,
(a, b, b) — spheroid semi-axes,
a_n, b_n — partial coefficients of the Mie theory,
A_s — generalized constant considering all damping processes including electron scattering at a particle boundary,
C_{abs}, C_{sca}, C_{ext} — absorption, scattering and extinction cross-sections, respectively,
c — speed of light in vacuum,
d — nanosphere or nanorod diameter,
$\mathbf{E}_0$ — incident field vector,
f — parameter determining the dependence of the plasmonic response on the optical susceptibility of the particle material,
f_{12} — volume fraction of the core in a two-layer particle,
f_g — volume fraction of gold in the gold nanoshell,
$k = 2\pi n_m/\lambda$ — wave number in a medium,
L — nanorod length,
L_a, L_b — geometric depolarization factors of a spheroid,
l_{eff} — effective mean free path of electrons,
$n_m = \sqrt{\varepsilon_m}$ — refractive index of the medium,
p — plasmon resonance parameter of a gold nanoshell,
P_{sca}, P_{ext} — scattering and extinction powers,
S — surface area of a particle,

v_F — Fermi velocity,

V — particle volume,

$x = ka$ — diffraction size parameter of a spherical particle of radius a,

α — polarizability of a spherical particle,

α_a, α_b — polarizability of a spheroid along a and b semi-axes,

α_R — modified polarizability of a spherical particle including radiative damping,

α_{12} — parameter determining the polarizability of a two-layer spherical particle,

γ_b — damping constant for bulk metal,

$\gamma_s = \gamma_s(\lambda_{eff})$ — size-dependent damping parameter,

γ_s^{rad} — radiative damping parameter,

γ_s^{surf} — damping parameter caused by electron scattering at the particle boundary,

γ_s^{CID} — chemical interface damping (CID) parameter,

$\varepsilon(\omega)$ — dielectric permittivity (dielectric function) of a particle at the angular optical frequency ω,

$\varepsilon'' = \mathrm{Im}(\varepsilon)$ — imaginary part of the dielectric permittivity,

ε_{ib} — contribution of interband transitions to the dielectric permittivity according to the Drude theory,

ε_m — dielectric permittivity of the medium,

$\varepsilon_r = \varepsilon/\varepsilon_m$ — relative dielectric permittivity of a particle,

$\varepsilon_p(\omega, l_{eff})$ — size-dependent dielectric permittivity of a particle at the angular optical frequency ω,

$\varepsilon_b(\omega)$ — dielectric function of the bulk material of a particle at the angular optical frequency ω,

$\Delta\varepsilon(\omega, l_{eff})$ — size-dependent correction for the bulk dielectric function,

ε_{av} — average polarizability of a multi-layer (two-layer) particle,

ε_1 and ε_2 — dielectric permittivities of the core and the shell of a two-layer particle,

$\eta = P_{sca}/P_{ext}$ — ratio of the scattering and extinction powers,

λ — light wavelength in vacuum,

$\lambda_p = 2\pi c/\omega_p$ — plasma oscillation wavelength,

λ_{PR} — plasmon resonance wavelength,

$\varphi(ka)$ — size-dependent polarizability correction factor,

$\varphi_0(x)$ — factor determining the size-dependent plasmon resonance shift of a spherical particle,

φ_{PR} — particle shape- and structure-dependent parameter determining the plasmon resonance wavelength,

$\varphi_{s,i}$ — parameter determining the plasmon resonance wavelength of a two-layer spherical particle,

χ — optical susceptibility of the particle material,

χ_c — parameter determining the degree of curvature of nanorod tips,

χ_d — parameter determining the decrease in the nanorod diameter in the middle in comparison with the tip diameter,

ω — angular optical frequency,

ω_p — angular plasma frequency,

ω_{PR} — angular plasmon resonance frequency.

11. References

1. L.A.Dykman, N.G.Khlebtsov. *Chem. Soc. Rev.*, **41**, 2256 (2012)
2. Y.Kumari, G.Kaur, R.Kumar, S.K.Singh, M.Gulati, R.Khursheed, A.Clarisse, K.Gowthamarajan, V.V.S.N.R.Karri, R.Mahalingam, D.Ghosh, A.Awasthi, R.Kumar, A.K.Yadav, B.Kapoor, P.K.Singh, K.Dua, O.Porwal. *Adv. Colloid Interface Sci.*, **274**, 102037 (2019)
3. S.A.Bansal, V.Kumar, J.Karimi, A.P.Singh, S.Kumar. *Nanoscale Adv.*, **2**, 3764 (2020)
4. J.Lou-Franco, B.Das, C.Elliott, C.Cao. *Nano-Micro Lett.*, **13**, 10 (2021)
5. M.Pohanka. *Mini-Rev. Med. Chem.*, **21**, 1085 (2021)
6. M.Yaseen, M.Humayun, A.Khan, M.Usman, H.Ullah, A.A.Tahir, H.Ullah. *Energies*, **14**, 1278 (2021)
7. *Colloidal Synthesis of Plasmonic Nanometals*. (Ed. L.Liz-Marzán). (New York: Jenny Stanford Publishing, 2021)
8. V.I.Roldugin. *Russ. Chem. Rev.*, **69**, 899 (2000)
9. E.K.Beloglazkina, A.G.Majouga, R.B.Rovashkina, N.V.Zyk, N.S.Zefirov. *Russ. Chem. Rev.*, **81**, 65 (2012)
10. W.Bian, Y.Wang, Z.Pan, N.Chen, X.Li, W.-L.Wong, X.Liu, Y.He, K.Zhang, Y.-J.Lu. *ACS Appl. Nano Mater.*, **4**, 11353 (2021)
11. A.B.Bucharskaya, N.G.Khlebtsov, B.N.Khlebtsov, G.N.Maslyakova, N.A.Navolokin, V.D.Genin, E.A.Genina, V.V.Tuchin. *Materials*, **15**, 1606 (2022)
12. L.A.Dykman, V.A.Bogatyrev. *Russ. Chem. Rev.*, **76**, 181 (2007)
13. L.A.Dykman, N.G.Khlebtsov. *Russ. Chem. Rev.*, **88**, 229 (2019)
14. F.Montanarella, M.V.Kovalenko. *ACS Nano*, **16**, 5085 (2022)
15. Yu.A.Krutyakov, A.A.Kudrinskiy, A.Yu.Olenin, G.V.Lisichkin. *Russ. Chem. Rev.*, **77**, 233 (2008)
16. B.K.Park, L.F.Drummy, R.C.Wadams, H.Koerner, D.Nepal, L.Fabris, R.A.Vaia. *Chem. Mater.*, **25**, 555 (2013)
17. J.E.Ortiz-Castillo, R.C.Gallo-Villanueva, M.J.Madou, V.H.Perez-Gonzalez. *Coord. Chem. Rev.*, **425**, 213489 (2020)
18. E.C.Dreaden, A.M.Alkilany, X.Huang, C.J.Murphy, M.A.El-Sayed. *Chem. Soc. Rev.*, **41**, 2740 (2012)
19. H.Chen, L.Shao, Q.Li, J.Wang. *Chem. Soc. Rev.*, **42**, 2679 (2013)
20. S.E.Lohse, C.J.Murphy. *Chem. Mater.*, **25**, 1250 (2013)
21. L.Vigderman, B.P.Khanal, E.R.Zubarev. *Adv. Mater.*, **24**, 4811 (2012)
22. Y.-Ch.Wang, É.Rhéaume, F.Lesage, A.Kakkar. *Molecules*, **23**, 2851 (2018)
23. Y.Xia, W.Li, C.M.Cobley, J.Chen, X.Xia, Q.Zhang, M.Yang, E.Ch.Cho, P.K.Brown. *Acc. Chem. Res.*, **44**, 914 (2011)
24. A.L.Siegel, G.A.Baker. *Nanoscale Adv.*, **3**, 3980 (2021)
25. L.M.Liz-Marzán. *Colloidal Synthesis of Plasmonic Nanometals. Ch. 4*. (Ed. L.Liz-Marzán). (New York: Jenny Stanford Publishing, 2021)
26. N.G.Khlebtsov, L.Lin, B.N.Khlebtsov, J.Ye. *Theranostics*, **10**, 2067 (2020)
27. C.F.Bohren, D.R.Huffman. *Absorption and Scattering of Light by Small Particles*. (New York: Wiley, 1983)
28. U.Kreibig, M.Volmer. *Optical Properties of Metal Clusters*. (Berlin: Springer-Verlag, 1995)
29. K.L.Kelly, E.Coronado, L.L.Zhao, G.C.Schatz. *J. Phys. Chem. B*, **107**, 668 (2003)
30. D.Pines. *Rev. Mod. Phys.*, **28**, 184 (1956)
31. E.C.Le Ru, P.G.Etchegoin. *Principles of Surface Enhanced Raman Spectroscopy and Related Plasmonic Effects*. (Amsterdam: Elsevier, 2009)
32. N.Khlebtsov. *Quantum Electron.*, **38**, 504 (2008)
33. L.G.Schulz. *J. Opt. Soc. Am.*, **44**, 357 (1954)
34. G.B.Irani, T.Huen, F.Wooten. *J. Opt. Soc. Am.*, **61**, 128 (1971)
35. M.Otter. *Z. Phys.*, **161**, 163 (1961)
36. L.R.Canfield, G.Hass, W.R.Hunter. *J. Phys. (Paris)*, **25**, 124 (1964)
37. H.-J.Hagemann, W.Gudat, C.Kunz. *Optical Constants from the far Infrared to the X-ray Region: Mg, Al, Cu, Ag, Bi, C, and Al_2O_3*. Deutsches Electronen-Synchrotron DESY SR-74/7, Hamburg, 1974
38. P.B.Johnson, R.W.Christy. *Phys. Rev. B*, **6**, 4370 (1972)

39. *Optical Properties of Metals. Vol. 2. Physics Data Series No. 18-2*. (Eds J.H.Weaver, C.Krafka, D.W.Lynch, E.E.Koch). (Karlsruhe: Fachinformationszentrum, 1981)
40. R.L.Olmon, B.Slovick, T.W.Johnson, D.Shelton, S.-H.Oh, G.D.Borema, M.B.Raschke. *Phys. Rev. B*, **86**, 235147 (2012)
41. N.G.Khlebtsov. *Phys. Chem. Chem. Phys.*, **23**, 23141 (2021)
42. N.G.Khlebtsov, V.A.Bogatyrev, L.A.Dykman, A.G.Melnikov. *J. Colloid Interface Sci.*, **180**, 436 (1996)
43. K.R.Brown, M.J.Natan. *Chem. Mater.*, **12**, 306 (1996)
44. K.R.Brown, M.J.Natan. *Langmuir*, **14**, 726 (1998)
45. B.D.Chithrani, A.A.Ghazani, W.C.W.Chan. *Nano Lett.*, **6**, 662 (2006)
46. D.Andreescu, T.K.Sau, D.V.Goia. *J. Colloid Interface Sci.*, **298**, 742 (2006)
47. M.Horisberger. In *Techniques in Immunocytochemistry*. (Eds G.R.Bullock, P.Petrusz). (London: Academic Press, 1985). P. 155
48. M.Slouf, R.Kuzel, Z.Z.Matej. *Kristallogr. Suppl.*, **23**, 319 (2006)
49. P.N.Njoki, I.-I.S.Lim, D.Mott, H.-Y.Park, B.Khan, S.Mishra, R.Sujakumar, J.Luo, C.-J.Zhong. *J. Phys. Chem. B*, **111**, 14664 (2007)
50. W.Haiss, N.T.K.Thanh, J.Aveard, D.G.Fernig. *Anal. Chem.*, **79**, 4215 (2007)
51. S.D.Perrault, W.C.W.Chan. *J. Am. Chem. Soc.*, **131**, 17042 (2009)
52. C.Ziegler, A.Eychmüller. *J. Phys. Chem. C*, **115**, 4502 (2011)
53. T.H.Do, T.H.L.Nghien, H.V.Chu. *J. Electron. Mater.*, **50**, 5514 (2021)
54. Y.Zheng, X.Zhong, Z.Li, Y.Xia. *Part. Part. Syst. Charact.*, **31**, 266 (2014)
55. Zhang, X.Li, C.Li, W.Cai, Y.Li. *Chem. Mater.*, **33**, 2593 (2021)
56. D.-K.Kim, Y.J.Hwang, C.Yoon, H.-O.Yoon, K.S.Chang, G.Lee, S.Lee, G.-R.Yi. *Phys. Chem. Chem. Phys.*, **17**, 20786 (2015)
57. URL: https://refractiveindex.info/?shelf=main&book=Au&-page= Rakic-BB
58. U.Kreibig, L.Genzel. *Sur. Sci.*, **156**, 678 (1985)
59. B.Foerster, A.Joplin, K.Kaefer, S.Celiksoy, S.Link, C.Sönnichsen, *ACS Nano*, **11**, 2886 (2017)
60. B.Foerster, V.A.Spata, E.A.Carte, C.Sönnichsen, S.Link. *Sci. Adv.*, **5**, eaav0704 (2019)
61. M.Xu, M.J.Dignam. *J. Chem. Phys.*, **96**, 3370 (1992)
62. A.Kawabata, R.Kubo. *J. Phys. Soc. Jpn.*, **21**, 1765 (1966)
63. A.A.Lushnikov, A.J.Simonov. *Z. Phys.*, **270**, 17 (1974)
64. E.A.Coronado, G.C.Schatz. *J. Chem. Phys.*, **119**, 3926 (2003)
65. A.V.Uskov, I.E.Protsenko, N.A.Mortensen, E.P.O'Reilly. *Plasmonics*, **9**, 185 (2013)
66. R.Ruppin, H.Yatoy. *Phys. Status Solidi, B*, **74**, 647 (1976)
67. W.A.Kraus, G.C.Schatz. *J. Chem. Phys.*, **79**, 6130 (1983)
68. N.G.Khlebtsov, S.V.Zarkov, V.A.Khanadeev, Y.A.Avetisyan. *Nanoscale*, **12**, 8343 (2020)
69. R.Fuchs. *Phys. Rev. B*, **11**, 1732 (1975)
70. B.N.Khlebtsov, A.G.Melnikov, V.P.Zharov, N.G.Khlebtsov. *Nanotechnology*, **17**, 1437 (2006)
71. V.Klimov. *Nano Plasmonics*. (New York: Jenny Stanford Publishing, 2014)
72. M.Meier, A.Wokaun. *Opt. Lett.*, **8**, 581 (1983)
73. I.L.Rasskazov, V.I.Zakomirnyi, A.D.Utyushev, P.S.Carney, A.Moroz. *J. Phys. Chem. C*, **125**, 1963 (2021)
74. N.G.Khlebtsov. *J. Quant. Spectrosc. Radiat. Transf.*, **123**, 184 (2013)
75. V.V.Tuchin. *Tissue Optics: Light Scattering Methods and Instruments for Medical Diagnosis*. (Bellingham: SPIE Press, 2000)
76. L.Cavigli, B.N.Khlebtsov, S.Centi, N.G.Khlebtsov, R.Pini, F.Ratto. *Nanomaterials*, **11**, 116 (2021)
77. J.Rodriguez-Fernandez, G.Perez-Juste, P.Mulvaney, L.M.Liz-Marzán. *J. Phys. Chem. B*, **109**, 14257 (2005)
78. V.A.Khanadeev, N.G.Khlebtsov, A.M.Burov, B.N.Khlebtsov. *Colloid J.*, **77**, 652 (2015)
79. X.Xu, M.B.Cortie. *Adv. Funct. Mater.*, **16**, 2170 (2006)
80. K.-S.Lee, M.A.El-Sayed. *J. Phys. Chem. B*, **109**, 20331 (2005)
81. B.Khlebtsov, V.Khanadeev, T.Pylaev, N.Khlebtsov. *J. Phys. Chem. C*, **115**, 6317 (2011)
82. H.Wang, D.W.Brandl, P.Nordlander, N.J.Halas. *Acc. Chem. Res.* **40**, 53 (2007)
83. D.Tzarouchis, A.Sihvola. *Appl. Sci.*, **8**, 184 (2018)
84. B.N.Khlebtsov, N.G.Khlebtsov. *J. Quant. Spectrosc. Radiat. Transf.*, **106**, 154 (2007)
85. L.A.Trachuk, S.A.Vrublevsky, B.N.Khlebtsov, A.G.Melnikov, N.G.Khlebtsov. *Proc. SPIE*, **5772**, 1 (2005)
86. B.N.Khlebtsov, V.P.Zharov, A.G.Melnikov, V.V.Tuchin, N.G.Khlebtsov. *Nanotechnology*, **17**, 5167 (2006)
87. M.B.Reinhard, M.Siu, H.Agarwal, A.P.Alivisatos, J.Liphardt. *Nano Lett.*, **5**, 2246 (2005)
88. R.T.Hill, J.J.Mock, A.Hucknall, S.D.Wolter, N.M.Jokerst, D.R.Smith, A.Chilkoti. *ACS Nano*, **6**, 9237 (2012)
89. G.A.Kelesidis, D.Gao, F.H.L.Starsich, S.E.Pratsinis. *Anal. Chem.*, **94**, 5310 (2022)
90. C.D.DeSouza, B.R.Nogueira, M.E.C.M.Rostelato. *J. Alloys Compd.*, **798**, 714 (2019)
91. P.Slepička, N.S.Kasálková, J.Siegel, Z.Kolská, V.Švorčík. *Materials*, **13**, 1 (2020)
92. I.Ielo, G.Rando, F.Giacobello, S.Sfameni, A.Castellano, M.Galletta, D.Drommi, G.Rosace, M.R.Plutino. *Molecules*, **26**, 5823 (2021)
93. T.K.Fai, P.V.Kumar. *Curr. Pharm. Des.*, **27**, 2482 (2021)
94. F.Ali, M.Hamza, M.Iqbal, B.Basha, N.Alwadai, A.Nazir. *Z. Phys. Chem.*, **236**, 291 (2021)
95. M.Wuithschick, A.Birnbaum, S.Witte, M.Sztucki, U.Vainio, N.Pinna, K.Rademann, F.Emmerling, R.Kraehnert, J.Polte. *ACS Nano*, 9, 7052 (2015)
96. D.P.Borowskaja. *Z. Immun. Exp. Ther.*, **82**, 178 (1934)
97. J.Turkevich, P.C.Stevenson, J.Hillier. *Discuss. Faraday Soc.*, **11**, 55 (1951)
98. G.Frens. *Nat. Phys. Sci.*, **241**, 20 (1973)
99. A.Chakraborty, T.Ahamd, B.B.Abdullah, S.Bhattacharjee. *Chem. Eng. Trans.*, **45**, 1939 (2015)
100. X.Ji, X.Song, J.Li, Y.Bai, W.Yang, X.Peng. *J. Am. Chem. Soc.*, **129**, 13939 (2007)
101. L.Shi, E.Buhler, F.Boué, F.Carn. *J. Colloid Interface Sci.*, **492**, 191 (2017)
102. M.Tran, R.De Penning, M.Turner, S.Padalkar. *Mater. Res. Express*, **3**, 105027 (2016)
103. S.Yazdani, A.Daneshkhah, A.Diwate, H.Patel, J.Smith, O.Reul, R.Cheng, A.Izadian, A.R.Hajrasouliha. *ACS Omega*, **6**, 16847 (2021)
104. J.Kimling, M.Maier, B.Okenve, V.Kotaidis, H.Ballot, A.Plech. *J. Phys. Chem. B*, **110**, 15700 (2006)
105. H.Xia, S.Bai, J.Hartmann, D.Wang. *Langmuir*, **26**, 3585 (2010)
106. M.Chen, Y.He, X.Liu, J.Zhu, R.Liu. *Powder Technol.*, **311**, 25 (2017)
107. N.G.Bastús, J.Comenge, V.Puntes. *Langmuir*, **27**, 11098 (2011)
108. J.P.Wilcoxon, P.P.Provencio. *J. Am. Chem. Soc.*, **126**, 6402 (2004)
109. S.Poklepovich-Caride, V.Oestreicher, M.M.Zalduendo, A.V.Bordoni, G.J.A.A.Soler-Illia, P.C.Angelomé. *Colloids Surf. A*, **646**, 128890 (2022)
110. D.Kumar, I.Mutreja, P.Sykes. *Nanotechnology*, **27**, 355601 (2016)
111. X.Liu, H.Xu, H.Xia, D.Wang. *Langmuir*, **28**, 13720 (2012)
112. X.Lu, A.Dandapat, Y.Huang, L.Zhang, Y.Rong, L.Dai, Y.Sasson, J.Zhang, T.Chen. *RSC Adv.*, **6**, 60916 (2016)
113. T.Liu, J.Wang, Z.Xie, L.Wan, J.Xiang, Y.Zhang, S.Luo, R.Bin, G.Liu. *Nanotechnology*, **31**, 405603 (2020)
114. Q.Ruan, L.Shao, Y.Shu, J.Wang, H.Wu. *Adv. Opt. Mater.*, **2**, 65 (2014)

115. L.Panariello, K.C.To, Z.Khan, G.Wu, G.Gkogkos, S.Damilos, I.P.Parkin, A.Gavriilidis. *Chem. Eng. J.*, **423**, 129069 (2021)
116. D.Goia, E.Matijević. *Colloids Surf. A*, **146**, 139 (1999)
117. W.Ahmed, İ.M.Öztürk, R.M.F.Iftikhar, A.Bek. *Mater. Chem. Phys.*, **278**, 125589 (2022)
118. C.R.Martin. *Chem. Mater.*, **8**, 1739 (1996)
119. B.M.I.Van der Zande, M.R.Boehmer, L.G.J.Fokkink, C.Schoenenberger. *J. Phys. Chem. B*, **101**, 852 (1997)
120. J.C.Hulteen, C.R.Martin. *J. Mater. Chem.*, **7**, 1075 (1997)
121. Y.-Y.Yu, S.-S.Chang, C.-L.Lee, C.R.C.Wang. *J. Phys. Chem. B*, **101**, 6661 (1997)
122. J.Pérez-Juste, I.Pastoriza-Santos, L.M.Liz-Marzán, P.Mulvaney. *Coord. Chem. Rev.*, **249**, 1870 (2005)
123. N.Jana, L.Gearheart, C.Murphy. *J. Phys. Chem. B*, **105**, 4065 (2001)
124. B.D.Busbee, S.O.Obare, C.J.Murphy. *Adv. Mater.*, **15**, 15414 (2003)
125. B.Nikoobakht, M.A.El-Sayed. *Chem. Mater.*, **15**, 1957 (2003)
126. L.Scarabelli, A.Sánchez-Iglesias, J.Pérez-Juste, L.M.Liz-Marzán. *J. Phys. Chem. Lett.*, **6**, 4270 (2015)
127. N.A.Salavatov, O.V.Dement'eva, A.I.Mikhailichenko, V.M.Rudoy. *Colloid J.*, **80**, 541 (2018)
128. X.Ye, C.Zheng, J.Chen, Y.Gao, C.B.Murray. *Nano Lett.*, **13**, 765 (2013)
129. L.Vigderman, E.R.Zubarev. *Chem. Mater.*, **25**, 1450 (2013)
130. M.R.K.Ali, B.Snyder, M.A.El-Sayed. *Langmuir*, **28**, 9807 (2012)
131. A.Liopo, S.Wang, P.J.Derry, A.A.Oraevsky, E.R.Zubarev. *RSC Adv.*, **5**, 91587 (2015)
132. B.N.Khlebtsov, V.A.Khanadeev, J.Ye, G.B.Sukhorukov, N.G.Khlebtsov. *Langmuir*, **30**, 1696 (2014)
133. B.N.Khlebtsov, V.A.Khanadeev, A.M.Burov, E.C.Le Ru, N.G.Khlebtsov. *J. Phys. Chem. C*, **124**, 10647 (2020)
134. A.V.Alekseeva, V.A.Bogatyrev, L.A.Dykman, B.N.Khlebtsov, L.A.Trachuk, A.G.Melnikov, N.G.Khlebtsov. *Appl. Opt.*, **44**, 6285 (2005)
135. B.N.Khlebtsov, V.A.Khanadeev, N.G.Khlebtsov. *J. Phys. Chem. C*, **112**, 12760 (2008)
136. F.Scaletti, C.S.Kim, L.Messori, V.M.Rotello. *MethodsX*, **1**, 118 (2014)
137. V.Sharma, K.Park, M.Srinivasarao. *Proc. Natl. Acad. Sci. USA*, **106**, 4981 (2009)
138. K.Park, H.Koerner, R.A.Vaia. *Nano Lett.*, **10**, 1433 (2010)
139. T.Thai, Y.Zheng, S.H.Nag, H.Ohshima, M.Altissimo, U.Bach. *Nanoscale*, **6**, 6515 (2014)
140. B.P.Khanal, E.R.Zubarev. *J. Am. Chem. Soc.*, **130**, 12634 (2008)
141. E.C.Dreaden, M.A.Mackey, X.Huang, B.Kang, M.A.El-Sayed. *Chem. Soc. Rev.*, **40**, 3391 (2011)
142. R.D.Near, S.C.Hayden, M.A.El-Sayed. *J. Phys. Chem. C*, **117**, 18653 (2013)
143. O.Miller, K.Park, R.A.Vaia. *Opt. Express*, **30**, 25061 (2022)
144. J.Zheng, X.Cheng, H.Zhang, X.Bai, R.Ai, L.Shao, J.Wang. *Chem. Rev.*, **121**, 13342 (2021)
145. H.S.Zhou, I.Honma, H.Komiyama, J.W.Haus. *Phys. Rev. B*, **50**, 12052 (1994)
146. S.Oldenburg, R.D.Averitt, S.Westcott, N.J.Halas. *Chem. Phys. Lett.*, **288**, 243 (1998)
147. J.L.West, N.J.Halas. *Annu. Rev. Biomed. Eng.*, **5**, 285 (2003)
148. W.Stöber, A.Fink, J.Bohn. *J. Colloid Interface Sci.*, **26**, 62 (1968)
149. S.Kalele, S.W.Gosavi, J.Urban, S.K.Kulkarni. *Curr. Sci.*, **91**, 1038 (2006)
150. V.A.Khanadeev, B.N.Khlebtsov, N.G.Khlebtsov. *J. Quant. Spectrosc. Radiat. Transf.*, **187**, 1 (2017)
151. D.H.Everett. *Basic Principles of Colloid Science*. (London: Royal Society of Chemistry, 1988)
152. B.E.Brinson, J.B.Lassiter, C.S.Levin, R.Bardhan, N.Mirin, N.J.Halas. *Langmuir*, **24**, 14166 (2008)
153. S.L.Westcott, S.J.Oldenburg, T.R.Lee, N.J.Halas. *Langmuir*, **14**, 5396 (1998)
154. D.B.Shenoy, A.A.Antipov, G.B.Sukhorukov, H.Möhwald. *Biomacromolecules*, **4**, 265 (2003)
155. D.G.Duff, A.Baiker, P.P.Edwards. *Langmuir*, **9**, 2301 (1993)
156. W.Shi, Y.Sahoo, M.T.Swihart, P.N.Prasad. *Langmuir*, **21**, 1610 (2005)
157. C.M.Aguirre, T.R.Kaspar, C.Radloff, N.J.Halas. *Nano Lett.*, **3**, 1707 (2003)
158. K.-T.Yong, Y.Sahoo, M.T.Swihart, P.N.Prasad. *Colloids Surf. A*, **290**, 89 (2006)
159. Y.Guan, Z.Xue, J.Liang, Z.Huang, W.Yang. *Colloids Surf. A*, **502**, 6 (2016)
160. Y.Sun, Y.Xia. *J. Am. Chem. Soc.*, **126**, 3892 (2004)
161. P.-Y.Silvert, R.Herrera-Urbina, K.Tekaia-Elhsissen. *J. Mater. Chem.*, **7**, 293 (1997)
162. X.Xia, Y.Xia. *Front. Phys.*, **9**, 378 (2014)
163. B.N.Khlebtsov, V.A.Khanadeev, I.L.Maksimova, G.S.Terentyuk, N.G.Khlebtsov. *Nanotechnologies in Russia*, **5**, 454 (2010)
164. J.Chen, F.Saeki, B.J.Wiley, H.Cang, M.J.Gobb, Z.-Y.Li, L.Au, H.Zhang, M.B.Kimmey, X.Li, Y.Xia. *Nano Lett.*, **5**, 473 (2005)
165. B.N.Khlebtsov, V.A.Khanadeev, E.V.Panfilova, O.A.Inozemtseva, A.M.Burov, N.G.Khlebtsov. *J. Quant. Spectrosc. Radiat. Transf.*, **121**, 23 (2013)
166. E.A.Maksimova, R.A.Barmin, P.G.Rudakovskaya, O.A.Sindeeva, E.S.Prikhozhdenko, A.M.Yashchenok, B.N.Khlebtsov, A.A.Solovev, G.Huang, Y.Mei, K.K.Dey, D.A.Gorin. *Micromachines*, **12**, 1161 (2021)
167. A.M.Schwartzberg, T.Y.Olson, C.E.Talley, J.Z.Zhang. *J. Phys. Chem. B*, **110**, 19935 (2006)
168. H.Yuan, C.G.Khoury, H.Hwang, C.M.Wilson, G.A.Grant, T.Vo-Dinh. *Nanotechnology*, **23**, 075102 (2012)
169. B.Khlebtsov, E.Panfilova, V.Khanadeev, N.Khlebtsov. *J. Nanopart. Res.*, **16**, 2623 (2014)
170. A.S.De Silva Indrasekara, S.F.Johnson, R.A.Odion, T.Vo-Dinh. *ACS Omega*, **3**, 2202 (2018)
171. C.S.Ah, S.D.Hong, D.J.J.Jang. *Phys. Chem. B*, **105**, 7871 (2001)
172. C.C.Huang, Y.Zang, H.T.Chang. *Langmuir*, **20**, 6089 (2004)
173. M.Liu, P.Guyot-Sionnest. *J. Phys. Chem. B*, **108**, 5882 (2004)
174. J.Becker, I.Zins, A.Jaka, Yu.Khalavka, O.Schubert, C.Sönnichsen. *Nano Lett.*, **8**, 1719 (2008)
175. B.N.Khlebtsov, V.A.Khanadeev, V.A.Bogatyrev, L.A.Dykman, N.G.Khlebtsov. *Nanotechnologies Russ.*, **4**, 453 (2009)
176. B.Khlebtsov, V.Khanadeev, N.Khlebtsov. *Phys. Chem. Chem. Phys.*, **12**, 3210 (2010)
177. N.Gandra, S.Singamaneni. *Adv. Mater.*, **25**, 1022 (2013)
178. B.Khlebtsov, V.Khanadeev, N.Khlebtsov. *Nano Res.*, **9**, 2303 (2016)
179. Y.Wang, Y.Wang, W.Wang, K.Sun, L.Chen. *ACS Appl. Mater. Interfaces*, **8**, 28105 (2016)
180. B.N.Khlebtsov, D.N.Bratashov, N.G.Khlebtsov. *J. Phys. Chem. C*, **122**, 17983 (2018)
181. B.N.Khlebtsov, Z.H.Liu, J.Ye, N.G.Khlebtsov. *J. Quant. Spectrosc. Radiat. Transf.*, **167**, 64 (2015)
182. Y.Yang, W.Wang, X.Li, W.Chen, N.Fan, C.Zou, X.Chen, X.Xu, L.Zhang, S.Huang. *Chem. Mater.*, **25**, 34 (2013)
183. S.Zhang, H.Lv, J.Zhao, M.Cheng, S.Sun. *Nanotechnology*, **30**, 265102 (2019)
184. B.Li, Y.Wang, J.He. *ACS Appl. Mater. Interfaces*, **11**, 7800 (2019)
185. W.Zhang, K.Cai, X.Li, J.Zhang, Z.Ma, M.F.Foda, Y.Mu, X.Dai, H.Han. *Theranostics*, **9**, 4971 (2019)
186. Y.Feng, Y.Chang, X.Sun, Y.Cheng, R.Zheng, X.Wu, L.Wang, X.Ma, X.Li, H. Zhang. *Biomater. Sci.*, **7** (4), 1448 (2019)

187. L.An, Y.Wang, J.Lin, Q.Tian, Y.Xie, J.Hu, S.Yang. *ACS Appl. Mater. Interfaces*, **11**, 15251 (2019)
188. X.-D.Liu, B.Chen, G.-G.Wang, S.Ma, L.Cheng, W.Liu, L.Zhou, Q.-Q.Wang. *Adv. Funct. Mater.*, **31**, 2104424 (2021)
189. A.O.Oladipo, T.C.Lebepe, V.Ncapayi, N.Tsolekile, S.Parani, S.P.Songca, S.Mori, T.Kodama, O.S.Oluwafemi. *Pharmaceutics*, **13**, 1359 (2021)
190. J.Ribera, C.Vilches, V.Sanz, I.DeMiguel, I.Portolés, B.Córdoba-Jover, E.Prat, V.Nunes, W.Jiménez, R.Quidant, M.Morales-Ruiz. *ACS Nano*, **15**, 7547 (2021)
191. A.S.Monem, F.A.-Z.Sayed, M.M.Rageh, N.Mohamed. *Life Sci.*, **257**, 118108 (2020)
192. Z.Mei, D.Gao, D.Hu, H.Zhou, T.Ma, L.Huang, X.Liu, R.Zheng, H.Zheng, P.Zhao, J.Zhou, Z.Sheng. *Biomaterials*, **251**, 120092 (2020)
193. K.R.Pulagam, M.Henriksen-Lacey, K.B.Uribe, C.Renero-Lecuna, J.Kumar, A.Charalampopoulou, A.Facoetti, N.Protti, V.Gómez-Vallejo, Z.Baz, V.Kumar, A.Sánchez-Iglesias, S.Altieri, U.Cossío, D.DiSilvio, A.M.Martínez-Villacorta, A.RuizDeAngulo, L.Rejc, L.M.Liz-Marzán, J.Llop. *ACS Appl. Mater. Interfaces*, **13**, 49589 (2020)
194. B.Seo, K.Lim, S.S.Kim, K.T.Oh, E.S.Lee, H.-G.Choi, B.S.Shin, Y.S.Youn. *Colloids Surf. B*, **179**, 340 (2019)
195. Q.Sun, J.Wu, L.Jin, L.Hong, F.Wang, Z.Mao, M.Wu. *J. Mater. Chem. B*, **8**, 7253 (2020)
196. X.Jin, H.Yang, Z.Mao, B.Wang. *J. Colloid Interface Sci.*, **601**, 714 (2021)
197. X.Liu, Q.Su, H.Song, X.Shi, Y.Zhang, C.Zhang, P.Huang, A.Dong, D.Kong, W.Wang. *Biomaterials*, **275**, 120921 (2021)
198. G.M.Proshkina, E.I.Shramova, M.V.Shilova, I.V.Zelepukin, V.O.Shipunova, A.V.Ryabova, S.M.Deyev, A.B.Kotlyar. *Cancers*, **13**, 5235 (2021)
199. C.Li, K.Feng, N.Xie, W.Zhao, L.Ye, B.Chen, C.-H.Tung, L.-Z.Wu. *ACS Appl. Nano Mater.*, **3**, 5070 (2020)
200. G.Liu, H.Liang, Y.He, L.Lu, L.Wang, P.Liu, K.Cai. *J. Mater. Chem. B*, **8**, 9686 (2020)
201. C.-C.Chuang, C.-C.Cheng, P.-Y.Chen, C.Lo, Y.-N.Chen, M.-H.Shih, C.-W.Chang. *Int. J. Nanomedicine*, **14**, 181 (2019)
202. S.Liao, W.Yue, S.Cai, Q.Tang, W.Lu, L.Huang, T.Qi, J.Liao. *Front. Pharmacol.*, **12**, 66412 (2021)
203. K.Bromma, D.B.Chithrani. *Nanomaterials*, **10**, 1671 (2020)
204. J.Liu, J.Shi, W.Nie, S.Wang, G.Liu, K.Cai. *Adv. Healthcare Mater.*, **10**, 2001207 (2021)
205. J.Chen, D.Wang, J.Xi, L.Au, A.Siekkinen, A.Warsen, Z.-Y.Li, H.Zhang, Y.Xia, X.Li. *Nano Lett.*, **7**, 1318 (2007)
206. A.Pakravan, M.Azizi, F.Rahimi, F.Bani, F.Mahmoudzadeh, R.Salehi, M.Mahkam. *Cancer Nanotechnol.*, **12**, 19 (2021)
207. Y.Hu, S.Huang, X.Zhao, L.Chang, X.Ren, X.Mei, Z.Chen. *Chem. Eng. J.*, **421**, 129744 (2021)
208. R.Robinson, W.Gerlach, H. Ghandehari. *J. Control. Release*, **220**, 245 (2015)
209. B.Pang, X.Yang, Y.Xia. *Nanomedicine (London)*, **11**, 1715 (2016)
210. S.Huang, Y.Liu, X.Xu, M.Ji, Y.Li, C.Song, S.Duan, Y.Hu. *J. Mater. Chem. B*, **6**, 2217 (2018)
211. S.Wang, Y.Song, K.Cao, L.Zhang, X.Fang, F.Chen, S.Feng, F.Yan. *Acta Biomater.*, **134**, 621 (2021)
212. Y.Wei, Z.Wang, J.Yang, R.Xu, H.Deng, S.Ma, T.Fang, J.Zhang, Q.Shen. *J. Colloid Interface Sci.*, **606**, 1950 (2022)
213. J.Qiu, M.Xie, T.Wu, D.Qin, Y.Xia. *Chem. Sci.*, **11**, 12955 (2020)
214. G.Chirico, M.Borzenkov, P.Pallavicini. *Gold Nanostars. Synthesis, Properties and Biomedical Application*. Springer, Berlin, 2015
215. B.M.Crawford, R.L.Shammas, A.M.Fales, D.A.Brown, S.T.Hollenbeck, T.Vo-Dinh, G.R.Devi. *Int. J. Nanomedicine*, **12**, 6259 (2017)
216. A.Espinosa, A.K.A.Silva, A.Sánchez-Iglesias, M.Grzelczak, C.Péchoux, K.Desboeufs, L.M.Liz-Marzán, C.Wilhelm. *Adv. Healthcare Mater.*, **5**, 1040 (2016)
217. T.Vo-Dinh, Y.Liu, B.M.Crawford, H.N.Wang, H.Yuan, J.K.Register, C.G.Khoury. *J. Immunol. Sci.*, **2**, 1 (2018)
218. Y.Liu, P.Chongsathidkiet, B.M.Crawford, R.Odion, C.A.Dechant, H.R.Kemeny, X.Cui, P.F.Maccarini, C.D.Lascola, P.E.Fecci, T.Vo-Dinh. *Immunotherapy*, **11**, 1293 (2019)
219. C.Vilches, R.Quidant. *Front. Nanosci.*, **16**, 307 (2020)
220. A.R.Rastinehad, H.Anastos, E.Wajswol, J.S.Winoker, J.P.Sfakianos, S.K.Doppalapudi, M.R.Carrick, C.J.Knauer, B.Taouli, S.C.Lewis, A.K.Tewari, J.A.Schwartz, S.E.Canfield, A.K.George, J.L.West, N.J.Halas. *Proc. Natl. Acad. Sci. USA*, **116**, 18590 (2019)
221. N.S.Abadeer, C.J.Murphy. *J. Phys. Chem. C*, **120**, 4691 (2016)
222. M.R.K.Ali, Y.Wu, M.A.El-Sayed. *J. Phys. Chem. C*, **123**, 15375 (2019)
223. L.Zhang, X.Ma, W.Zhou, Q.Wu, J.Yan, X.Xu, B.Ghimire, J.M.Rosenholm, J.Feng, D.Wang, H.Zhang. *Mater. Today Adv.*, **13**, 100199 (2022)
224. L.A.Dykman, N.G.Khlebtsov. *Biomed. Opt. Express*, **10**, 3152 (2019)
225. M.Yuan, S.Xu, Q.Zhang, B.Zhao, B.Feng, K.Ji, L.Yu, W.Chen, M.Hou, Y.Xu, X.Fu. *Chem. Eng. J.*, **394**, 124874 (2020)
226. T.Zhao, X.Shen, L.Li, Z.Guan, N.Gao, P.Yuan, S.Q.Yao, Q.-H.Xu, G.Q.Xu. *Nanoscale*, **4**, 7712 (2012)
227. C.Jiang, T.Zhao, P.Yuan, N.Gao, Y.Pan, Z.Guan, N.Zhou, Q.-H.Xu. *ACS Appl. Mater. Interfaces*, **5**, 4972 (2013)
228. R.Vankayala, Y.K.Huang, P.Kalluru, C.S.Chiang, K.C.Hwang. *Small*, **10**, 1612 (2014)
229. J.Lv, X.Zhang, N.Li, B.Wang, S.He. *RSC Adv.*, **5**, 81897 (2015)
230. R.Vankayala, C.-L.Kuo, A.Sagadevan, P.-H.Chen, C.-S.Chiang, K.C.Hwang. *J. Mater. Chem. B*, **1**, 4379 (2013)
231. R.Vankayala, C.-C.Lin, P.Kalluru, C.-S.Chiang, K.C.Hwang. *Biomaterials*, **35**, 5527 (2014)
232. J.H.Correia, J.A.Rodrigues, S.Pimenta, T.Dong, Z.Yang. *Pharmaceutics*, **13**, 1332 (2021)
233. O.Dahl. In *Application of Hyperthermia in the Treatment of Cancer. Recent Results in Cancer Research*. (Eds R.D.Issels, W.Wilmanns). (Berlin: Springer-Verlag, 1988)
234. M.Urano, M.Kuroda, Y.Nishimura. *Int. J. Hyperthermia*, **15**, 79 (1999)
235. T.F.Gajewski, H.Schreiber, Y.X.Fu. *Nat. Immunol.*, **14**, 1014 (2013)
236. V.D.Turubanova, T.A.Mishchenko, I.V.Balalaeva, I.Efimova, N.N.Peskova, L.G.Klapshina, S.A.Lermontova, C.Bachert, O.Krysko, M.V.Vedunova, D.V.Krysko. *Sci. Rep.*, **11**, 7205 (2021)
237. Y.Zhang, T.Song, T.Feng, Y.Wan, N.T.Blum, C.Liu, C.Zheng, Z.Zhao, T.Jiang, J.Wang, Q.Li, J.Lin, L.Tang, P.Huang. *Nano Today*, **35**, 100987 (2020)
238. Y.Liu, E.Chorniak, R.Odion, W.Etienne, S.K.Nair, P.Maccarini, G.M.Palmer, B.A.Inman, T.Vo-Dinh. *Nanophotonics*, **10**, 3295 (2021)
239. A.Chen, L.Wu, Y.Luo, S.Lu, Y.Wang, Z.Zhou, D.Zhou, Z.Xie, J.Yue. *Small*, **18**, 2200993 (2022)
240. L.A.Dykman, N.G.Khlebtsov. *Chem. Sci.*, **8**, 1719 (2017)
241. L.A.Dykman, S.A.Staroverov, A.S.Fomin, V.A.Khanadeev, B.N.Khlebtsov, V.A.Bogatyrev. *Int. Immunopharmacol.*, **54**, 163 (2018)
242. B.-K.Jung, Y.K.Lee, J.Hong, H.Ghandehari, C.-O.Yun. *ACS Nano*, **10**, 10533 (2016)
243. G.Chen, L.Ding, P.Wu, Y.Zhou, M.Sun, K.Wang, D.Oupicky. *Polym. Adv. Technol.*, **29**, 2593 (2018)
244. L.M.Chong, D.J.H.Tng, L.L.Y.Tan, M.L.K.Chua, Y.Zhang. *Appl. Phys. Rev.*, **8**, 041322 (2021)
245. R.Cai, H.Xiang, D.Yang, K.-T.Lin, Y.Wu, R.Zhou, Z.Gu, L.Yan, Z Y.Zhao, W.Tan. *J. Am. Chem. Soc.*, **143**, 16113 (2021)

246. Z.Kayani, N.Islami, N.Behzadpour, N.Zahraie, S.Imanlou, P.Tamaddon, F.Salehi, F.Daneshvar, G.Perota, E.Sorati, S.Mohammadi, N.Sattarahmady. *J. Drug Deliv. Sci. Technol.*, **65**, 102689 (2021)
247. L.A.Lyon, C.D.Keating, A.P.Fox, B.E.Baker, L.He, S.R.Nicewarner, S.P.Mulvaney, M.J.Natan. *Anal. Chem.*, **70**, 341 (1998)
248. K.Kneipp, H.Kneipp, I.Itzkan, R.R.Dasari, M.S.Feld. *J. Phys.: Condens. Matter*, **14**, 597 (2002)
249. K.Kneipp, H.Kneipp, I.I tzkan, R.R.Dasari, M.S.Feld. *Chem. Rev.*, **99**, 2957 (1999)
250. T.Vo-Dinh. *Trends Anal. Chem.*, **17**, 557 (1998)
251. S.C.Boca, C.Farcau, S.Astilean. *Nucl. Instrum. Methods Phys. Res. B*, **267**, 406 (2009)
252. L.Rodríguez-Lorenzo, R.A.Álvarez-Puebla, I.Pastoriza-Santos, S.Mazzucco, O.Stéphan, M.Kociak, L.M.Liz-Marzán, F.J.deAbajo. *J. Am. Chem. Soc.*, **131**, 4616 (2009)
253. J.Reguera, J.Langer, D.J.de Aberasturi, L.M.Liz-Marzán. *Chem. Soc. Rev.*, **46**, 3866 (2017)
254. F.Tian, F.Bonnier, A.Casey, A.E.Shanahan, H.J.Byrne. *Anal. Methods*, **6**, 9116 (2014)
255. Q.Zhang, N.Large, H.Wang. *ACS Appl. Mater. Interfaces*, **6**, 17255 (2014)
256. A.K.Samal, L.Polavarapu, S.Rodal-Cedeira, L.M.Liz-Marzán, J.Pérez-Juste, I.Pastoriza-Santos. *Langmuir*, **29**, 15076 (2013)
257. Y.Ma, J.Zhou, W.Zou, Z.Jia, L.Petti, P.Mormile. *J. Nanosci. Nanotechnol.*, **14**, 4245 (2014)
258. A.M.Fales, H.Yuan, T.Vo-Dinh. *J. Phys. Chem. C*, **118**, 3708 (2014)
259. S.-J.Ding, J.Zhu. *Appl. Surf. Sci.*, **357**, 487 (2015)
260. Y.Wang, B.Yan, L.Chen. *Chem. Rev.*, **113**, 1391 (2013)
261. Z.Ye, L.Lin, Z.Tan, Y.-J.Zeng, S.Ruan, J.Ye. *Appl. Surf. Sci.*, **487**, 1058 (2019)
262. B.Andreiuk, F.Nicolson, L.M.Clark, S.R.Panikkanvalappil, K.M.Rashidian, S.Harmsen, M.F.Kircher. *Nanotheranostics*, **6**, 10 (2022)
263. T.Vo-Dinh, Y.Liu, A.M.Fales, H.Ngo, H.-N.Wang, J.K.Register, H.Yuan, S.J.Norton, G.D.Griffin. *Wiley Interdisc. Rev. Nanomed. Nanobiotechnol.*, **7**, 17 (2015)
264. L.A.Lane, X.Qian, S.Nie. *Chem. Rev.*, **115**, 10489 (2015)
265. A.-I.Henry, B.Sharma, M.F.Cardinal, D.Kurouskiffi, R.P.VanDuyne. *Anal. Chem.*, **88**, 6638 (2016)
266. C.Zong, M.Xu, L.-J.Xu, T.Wei, X.Ma, X.-S.Zheng, R.Hu, B.Ren. *Chem. Rev.*, **118**, 4946 (2018)
267. H.Chen, Z.Cheng, X.Zhou, R.Wang, F.Yu. *Anal. Chem.*, **94**, 143 (2022)
268. C.Wen, L.Wang, L.Liu, X.-C.Shen, H.Chen. *Chem. – Asian J.*, **17**, e202200014 (2022)
269. D.Cialla-May, C.Krafft, P.Rösch, T.Deckert-Gaudig, T.Frosch, I.J.Jahn, S.Pahlow, C.Stiebing, T.Meyer-Zedler, T.Bocklitz, I.Schie, V.Deckert, J.Popp. *Anal. Chem.*, **94**, 86 (2022)
270. G.J.Hutchings, M.Haruta. *Appl. Catal. A*, **291**, 2 (2005)
271. S.B.Alyabyev, I.P.Beletskaya. *Russ. Chem. Rev.*, **86**, 689 (2017)
272. S.B.Alyabyev, I.P.Beletskaya. *Russ. Chem. Rev.*, **89**, 491 (2020)
273. S.B.Alyabyev, I.P.Beletskaya. *Russ. Chem. Rev.*, **87**, 984 (2018)
274. M.Stratakis, H.Garcia. *Chem. Rev.*, **112**, 4469 (2012)
275. T.Tabakova. *Front. Chem.*, **7**, 517 (2019)
276. M.Sankar, Q.He, R.V.Engel, M.A.Sainna, A.J.Logsdail, A.Roldan, D.J.Willock, N.Agarwal, C.J.Kiely, G.J.Hutchings. *Chem. Rev.*, **120**, 3890 (2020)
277. P.R.Murthy, P.Selvam. *Chem. Rec.*, **19**, 1913 (2019)
278. E.Cortés. *Adv. Opt. Mater.*, **5**, 1700191 (2017)
279. Z.Gong, J.Ji, J.Wang. *Catalysts*, **9**, 193 (2019)
280. Z.Li, D.Kurouski. *Nanophotonics*, **10**, 1657 (2021)
281. P.S.Kumar, I.Pastoriza-Santos, B.Rodriguez-Gonzalez, F.J.G.DeAbajo, L.M.Liz-Marzán. *Nanotechnology*, **19**, 015606 (2007)
282. S.Wang, P.Huang, L.Nie, R.Xing, D.Liu, Z.Wang, J.Lin, S.Chen, G.Niu, G.Lu, X.Chen. *Adv. Mater.*, **25**, 3055 (2013)
283. V.Alimardani, G.Farahavar, S.Salehi, S.Taghizadeh, M.R.Ghias, S.S.Abolmaali. *Front. Mater. Sci.*, **15**, 494 (2021)
284. G.vonMaltzahn, J.-H.Park, A.Agrawal, N.K.Bandaru, S.K.Das, M.J.Sailor, S.N.Bhatia. *Cancer Res.*, **69**, 3892 (2009)
285. A.K.Rengan, G.Kundu, R.Banerjee, R.Srivastava. *Part. Part. Syst. Charact.*, **31**, 398 (2014)
286. V.P.Pattani, J.W.Tunnell. *Lasers Surg. Med.*, **44**, 675 (2012)
287. D.K.Roper, W.Ahn, M.Hoepfner. *J. Phys. Chem. C*, **111**, 3636 (2007)
288. W.Yang, B.Xia, L.Wang, S.Ma, H.Liang, D.Wang, J.Huang. *Mater. Today Sustain.*, **13**, 100078 (2021)
289. T.Pylaev, E.Vanzha, E.Avdeeva, B.Khlebtsov, N.Khlebtsov. *J. Biophotonics*, **12**, e201800166 (2019)
290. L.Yang, J.Wang, L.Sun, Y.Zhang, P.Huang, J.Guo. *Nano*, **16**, 2150037 (2021)
291. Y.Wang, K.C.L.Black, H.Luehmann, W.Li, Y.Zhang, X.Cai, D.Wan, S.-Y.Liu, M.Li, P.Kim, Z.-Y.Li, L.V.Wang, Y.Liu, Y.Xia. *ACS Nano*, **7**, 2068 (2013)
292. N.G.Khlebtsov, L.A.Dykman. *Chem. Soc. Rev.*, **40**, 1647 (2009)
293. N.Bertrand, J.Wub, X.Xu, N.Kamaly, O.C.Farokhzad. *Adv. Drug Delivery Rev.*, **66**, 2 (2014)
294. F.Danhier. *J. Control. Release*, **244**, 108 (2016)